This is the peer-reviewed, final accepted version for American Mineralogist, published by the Mineralogical Society of America.
The published version is subject to change. Cite as Authors (Year) Title. American Mineralogist, in press.
DOI: https://doi.org/10.2138/am-2021-7733. http://www.minsocam.org/

Revision #2

PETROLOGIC EVOLUTION OF BONINITE LAVAS FROM THE IBM FORE-ARC, IODP EXPEDITION 352: EVIDENCE FOR OPEN-SYSTEM PROCESSES DURING EARLY SUBDUCTION ZONE MAGMATISM

Jesse L. Scholpp[a], Jeffrey G. Ryan[a], John W. Shervais[b], Ciprian Stremtan[c], Martin Rittner[d], Antonio Luna[a], Stephen A. Hill[a], Zachary D. Atlas[a], Bradford C. Mack[a]

[a] School of Geosciences, University of South Florida, 4202 E. Fowler Avenue, NES 107, Tampa, FL, 33620 USA

[b] Department of Geology, Utah State University, 4505 Old Main Hill, Logan, UT, 84322 USA

[c] Teledyne CETAC Technologies, 14306 Industrial Road, Omaha, NE, 68144 USA

[d] TOFWERK AG, Schorenstrasse 39, 3645 Thun, Switzerland

ABSTRACT

Boninite samples from several intervals within Hole U1439C, recovered during IODP Expedition 352, show highly variable mineral chemistries that imply complex crystallization histories. Small pyroxene grains show oscillatory zoning with cores and zones ranging from pigeonite to augite. Late crystallizing augite has highly variable Al_2O_3 contents (1.9-13.7 wt%.) and Ca-Tschermak component contents (3-13 mol%), which reflect disequilibrium conditions. Large, euhedral, low-Ca pyroxene (i.e., enstatite/clinoenstatite) crystals exhibit complex sector and oscillatory zoning patterns. Cr-rich spinel is found as inclusions both in olivine and low-Ca pyroxene. Early-crystallized olivine phenocrysts have embayed and reacted margins, and some early-crystallized olivines exhibit zoning. A few olivines have multiple zones, with both normal and reverse zoning between Fo_{86-92}. Olivine xenocrysts also have embayed and reacted margins; however, xenocrysts do not exhibit chemical zoning patterns and have consistent Fo_{88} compositions. Disequilibrium crystallization of pyroxene rims reflects rapid cooling during eruption. Sector zoning in low-Ca pyroxenes is the result of crystallization during periods of moderate undercooling between mixing events. Oscillatory, normal, and reverse zoning in olivine and pyroxene appears to have formed in response to multi-stage magma mingling or

mixing processes, which introduced additional Ca, Fe, Ti, and Al into parental boninitic melts. The presence of olivine xenocrysts andorthopyroxene indicate equilibrium at 2-4 kbar (Whattam et al. 2020) indicates that boninite magma mixing events likely occurred within shallow magma chambers containing olivine-rich cumulate piles. Large mixing events probably destabilized the magma chamber, resulting in devolatilization and eruption. In contrast, small mixing events lacked the energy to destabilize the chamber, resulting in repeated compositional oscillations in minerals affected by multiple small mixing events.

Keywords: Boninite, Magma Mixing, Olivine, Pyroxene, Zoning

INTRODUCTION

Boninites are unusual, high SiO_2 (>52 wt%), high MgO (>8 wt%), and low TiO_2 (<0.5 wt%) mafic rocks that are distinctively associated with subduction processes, in particular the unusual processes and phenomena of subduction initiation (Pearce and Reagan 2019; Shervais et al. 2021). They are commonly found in the forearcs in western Pacific arc systems such as the Izu-Bonin-Mariana (IBM) system (the type locality of boninite) and Tonga-Kermadec arc system (Dietrich et al. 1978; Bloomer et al. 1979; Meijer 1980; Meijer et al. 1982; Crawford 1989; Arculus et al. 1992; Dobson et al. 2006; Meffre et al. 2012) and have been observed actively erupting in the Lau Basin (Falloon and Crawford 1991; Falloon et al. 1992; Resing et al. 2011). Boninites are also common in ophiolites such as Troodos (Cyprus), Samail (Oman), Thetford Mines (Canada), Betts Cove (Canada), and Koh (New Caledonia) (Cameron 1985; Kyser et al. 1986; Meffre et al. 1996; Bedard et al. 1998; Wyman 1999; Ishikawa et al. 2002, 2005; Page et al. 2008, 2009). "Boninite-like" veins have also been found in some mantle xenoliths from Kamchatka and the West Bismarck arc (Benard et al. 2016, 2018).

Boninites associated with the Izu-Bonin fore-arc reflect the evolution of magmatic processes associated with subduction initation, in which the foundering of old oceanic lithosphere leads to upwelling of asthenospheric mantle (e.g., Stern and Bloomer 1992; Reagan et al 2010; Reagan et al. 2017). Competing models exist as to how boninites form in this setting. Pearce et al. (1999) suggests that boninites result from mixing between partial melts from gabbroic veins in the shallow mantle and melts from the upwelling asthenosphere. Recent studies have contended that mantle upwelling associated with initial plate foundering results in decompression melting that produces voluminous tholeiitic basalts (fore-arc basalts (FAB); Reagan et al. 2010, 2017, 2019; Shervais et al. 2019). This basaltic melting extensively depletes this upwelling mantle, which is then fluxed with a high-temperature fluid phase from the downgoing slab, triggering continued melting and the formation of boninite magma (Li et al. 2019; Reagan et al. 2017, 2019; Shervais et al 2021; Coulthard et al 2021).

Past studies of western Pacific boninites have focused on their unusual whole-rock major and trace element chemistries and isotopic compositions (Hickey and Frey 1982; Bloomer and Hawkins 1987; Falloon and Crawford 1991; Arculus et al. 1992; Murton et al. 1992; Pearce et al. 1992, 1999; Dobson et al. 2006; Shervais et al 2021; Coulthard et al 2021). Detailed mineralogical studies of fresh boninite volcanic sections have been comparatively rare given uncommon land-based exposures and/or limited dredging or submersible recovery. As the mineralogical features in boninites can directly reflect the conditions of their crystallization and melting, understanding these features can provide important insights into the conditions of magma formation and volcanism as subduction begins. IODP Expedition 352 cored over 800 m of the volcanic basement of the Izu-Bonin forearc at two different sites, recovering over 460 m of boninite and high-Mg andesite core (Reagan et al. 2015, 2017). These samples represent the

most complete stratigraphic sequence of boninites recovered in any forearc setting. We have examined the mineralogical features of a suite of Expedition 352 boninites from Hole U1439C, using thin-section petrography and mineral chemistry, to place new constraints on the petrogenesis of these lavas. Our results point to a significant role for open-system magmatic processes, both among different boninitic lava types and spatially associated boninitic differentiates.

Past mineralogical and petrologic studies of Izu-Bonin boninites

Johannsen (1937) reported on high-Mg/high-Si volcanic rocks in the Bonin (Ogasawara) Islands; however, systematic petrologic and geochemical studies of these lavas did not occur until much later (e.g., Kuroda and Shiraki 1975; Hickey and Frey 1982; Cameron et al. 1983). Meijer (1980, 1982) proposed the existence of a boninite suite associated with fore-arc volcanism based on discoveries by the Deep Sea Drilling Program (DSDP) and dredging. The first full petrologic study was performed by Umino (1986), who distinguished two major types and five subtypes of boninite, and, based in part on zoned pyroxene crystals, argued for their evolution in a dynamic magma chamber, with the mixing of more- and less-evolved boninitic magmas to produce at least one of the lava subtypes. Taylor et al. (1994) examined trace element compositions in Chichijima boninite, noting their unusually low Ti/Zr and Sm/Zr ratios, which were inferred to reflect chemical inputs from amphibolitic, probably slab-related, sources. Dobson et al. (2006) conducted an extensive study of the Chichijima volcanics, documenting related rock types ranging from Mg-rich boninite to rhyolite, and the presence of high-Ca clinopyroxene in all the Chichijima volcanic rock types. Li et al. (2013) described boninite and differentiates from Hahajima seamount occurring in association with adakites, which point to high-temperature conditions on the slab. ODP Leg 125 (Hole 786A) drilled a boninitic volcanic

sequence in a basement high near the Izu-Bonin trench at Site 786, NE of Sumisu-Jima island, that appeared to be lithologically and compositionally similar to both Chichijima Island boninites, and to Mariana boninites encountered during DSDP Site 458 (Meijer et al. 1982; Arculus et al. 1992).

IODP Expedition 352

A primary objective of IODP Expedition 352 was to recover a complete stratigraphic section through the igneous crust exposed near the trench in the Izu-Bonin fore-arc, as identified during a series of Shinkai dive expeditions (e.g., Ishizuka et al. 2011). Four sites were drilled, two into boninites (Sites U1439 and U1442), and two into fore-arc basalts (FAB) (Sites U1440 and U1441), with 20-30% recovery in the boninites, and ≤10% in the basalts (Reagan et al. 2015; Figures 1 & 2). In one fore-arc basalt site (U1440) and one boninite site (U1439), rocks with diabasic textures were penetrated, indicating that the transition from tholeiite to boninite may reflect a shift in the locus of magmatism, at odds with the ostensibly vertical basalt-to-boninite sequences encountered in the Troodos ophiolite (Reagan et al. 2017). However, Reagan et al. (2017) state that a direct transition from FAB to boninite melt compositions at the original spreading center is the preferred hypothesis.

Sites U1439 and U1442, though less than 1 km apart, reflect remarkably different stratigraphies (Figure 1). Hole U1442A is dominated by distinctive low-Si boninite (LSB), and boninitic differentiates (terminology after Kanayama et al. 2012, 2013; and Pearce and Reagan 2019), occurring as lava flows and hyaloclastites, capped with a sequence of late-stage high-Si boninite (HSB) hyaloclastites and lava flows, which are mineralogically and chemically similar to those found on Chichijima and other IBM sites. In contrast, Site U1439 (Holes U1439A and U1439C) reflects greater lithologic diversity, with diabasic rocks that appear to represent

boninite feeder dikes overlain by LSB and differentiates, which are themselves separated from overlying HSB by a layer of what was described as basaltic boninite (Reagan et al. 2015, Figure 2). Also evident in the U1439C cores are what were described as "magma mingling" textures, interpreted as intercalated evolved and primitive boninitic melts (Reagan et al. 2015), pointing to complexities in the generation and evolution of the Expedition 352 boninitic magmas.

SAMPLES AND METHODS

The IODP Expedition 352 boninite sequences were initially targeted for examination as part of a multi-year, course-based undergraduate research experience (CURE) for University of South Florida Geology undergraduates, overseen by co-author Ryan as part of an ongoing educational investigation into the use of research microbeam instrumentation in geoscience courses (see Ryan 2013). Boninite samples were selected to provide representative coverage of the different lithologies at each site and were also chosen to be comparatively crystal-rich, to facilitate petrographic and microprobe examination of the different crystallizing phases encountered in the samples. Thirty samples from Holes U1442A, U1439A, and U1439C were obtained from the IODP Core Repository at Kochi, Japan specifically for classroom study, and an additional fifteen samples came from the samples selected by Ryan for post-cruise geochemical study. Polished thin-sections were prepared from each of the samples for polarized-light petrographic analysis. Initial petrographic analyses of the samples were conducted during the course by participating students, who also helped to identify petrographically interesting samples for subsequent mineral chemistry studies. Four of the forty five samples (U1439C-2R3W 2-3, U1439C-15R1W 8-10, U1439C-19R2W 46-48, and U1439C-25R2W 18-19) will be the primary focus throughout this paper do to the mineral zoning and overgrowth texture they exhibit.

Micro-imaging and mineral chemistry measurements were conducted using the JEOL 8900R Superprobe EPMA system of the Florida Center for Analytical Electron Microscopy (FCAEM) at Florida International University, and the Cameca SXFive of the Center for Material Characterization at Boise State University. Samples were explored in electron backscatter mode, with quick energy dispersive spectrometer (EDS) measurements to identify major mineral phases. For quantitative WDS mineral analyses, operating conditions were a 15 kV accelerating voltage and a 20 nA beam current, 15 s count time per element, with a spot size of 1-2 μm on the JEOL 8900R Superprobe and 5-10 μm on the Cameca SXfive. The elements Si, Al, Fe, Mg, Ca, Mn, Na, K, Ti, and Cr, were routinely measured on all samples on both instruments. For the JEOL 8900R Superprobe, a selection of mineral standards from SPI, Inc., and Micro-Analysis Consultants, Ltd. were used to calibrate WDS measurements of unknowns (fayalite, olivine, Cr-diopside, An65 plagioclase, kaersutite, augite, enstatite, and chromite). Re-calculation or re-analysis using a smaller set of compositionally matched standards after minerals were identified (e.g., the SPI, Inc. olivine #AS5200-AB standard was used to re-calculate olivine analysis, the SPI, Inc. diopside #AS5130-AB standard was used to re-calculate pyroxene analysis; Online Material[1] Table OM1). For the Cameca SXFive a selection of synthetic mineral standards, as well as natural mineral and glass standards from the Smithsonian Institution, Harvard Mineralogical Museum, and the United States Geological Survey (USGS) were used to calibrate WDS measurements (San Carlos olivine, chromite, sillimanite, diopside, synthetic tephroite, synthetic fayalite, synthetic rutile, and Amelia albite). A similar re-analysis procedure was also used on the Cameca SXfive, for olivine analysis the San Carlos olivine NMNH-111312-44 standard was used and for pyroxene analysis the diopside NMNH-117733 standard was used (Online Material[1] Table OM1). EPMA measurements were used to confirm microscope-based

phase identifications, to identify important minor phases (Cr rich spinels, and rare ilmenites and apatites), and to characterize the mineral zoning and overgrowth textures that were encountered in some of the samples.

Elemental maps were created using the Cameca SXFive at the Center for Material Characterization at Boise State University and the TOFWERK icpTOF 2R at TOFWERK AG in Switzerland. The instrumental setup used for the laser ablation inductively coupled mass spectrometry imaging (LA ICP-MS) experiments consisted of a laser ablation system (excimer ArF 193 nm wavelength, Teledyne CETAC Analyte G2) equipped with an ultra-fast laser ablation chamber (van Malderen et al., 2020) and interfaced with a time-of-flight mass spectrometer (icpTOF 2R). The coupling of the two instruments was carried out via the Aerosol Rapid Introduction System (ARIS), which allowed the acquisition of full pulse signals of less than 3 ms (FW0.1M). The instrumental operating conditions are listed in the supplemental data (Online Material[1] Table OM2). The resulting images were generated using the HDIP software (van Malderen, 2017).

RESULTS

Petrography

The common phenocryst assemblage in the boninites examined in this study is low-Ca pyroxene (enstatite and clinoenstatite) + olivine, in a groundmass of later-formed acicular crystals of clinoenstatite, pigeonite, and high-Ca pyroxene in a glassy or crystalline matrix (Table 1, Online Material[1] Fig. S1). Some enstatite crystals enclose small olivine grains, indicating that these enstatites formed in part via the peritectic reaction of olivine. Some HSB samples lack olivine, consisting exclusively of low-Ca pyroxenes and groundmass clinopyroxene in a glassy or crystalline matrix. In more differentiated samples (high-Mg andesites and dacites),

the primary crystallizing phases are augitic clinopyroxene and plagioclase, with rare grains of ilmenite and apatite. Olivine grains are typically rounded and embayed, indicating partial resorption associated with the growth of enstatite and clinoenstatite at lower pressures. Olivine xenocrysts were observed in sample U1439C-25R2W18-19; these xenocrysts are much larger (>6 mm) than the primary olivine phenocrysts (≤1.5 mm) observed in this sample and exhibit resorbed textures. Red to purple chromium-rich spinel is a common accessory mineral in boninite, often found enclosed within larger olivine and (rarely) enstatite and clinoenstatite crystals (but never within pigeonite grains), and as free grains within the sample matrices (Figure S.1). Melt inclusions with vapor bubbles and crystals nucleating from the walls of the inclusion have also been observed in some samples (Figure S.2c.-2f.).

Mineral chemistry

Table 2 presents typical major element compositions for the Expedition 352 boninite phenocryst phases. Enstatite and clinoenstatite phenocrysts vary from $En_{80\text{-}86}$, with $Wo_{3\text{-}5}$ (Fig. 3), broadly similar to those reported from Chichijima by Umino (1986). We did not see enstatite rimming clinoenstatite, as was reported by Dobson et al. (2006), but instead found that most of our low-Ca pyroxene phenocrysts were homogeneous, with optical characteristics suggestive in most cases of enstatite. The more calcic clinopyroxene compositions in our samples are pigeonite ($En_{70\pm3}Fs_{12\pm0.6}Wo_{16\pm2}$) and augite ($En_{42\pm9}Fs_{14\pm4}Wo_{36\pm4.5}$). Augite from the most differentiated high-Mg andesite is typically $En_{50\pm3}Fs_{7\pm0.8}Wo_{42\pm2}$, in association with late-crystallized $An_{81\text{-}83}$ plagioclase.

Olivine phenocryst compositions range from $Fo_{86\text{-}92}$, similar to those reported at Chichijima by Umino (1986) and Dobson et al. (2006). Olivine xenocrysts in sample U1439C-25R2W18-19 exhibit consistent compositions of Fo_{88} (Table 3), while olivine phenocrysts from

the sample have compositions between Fo_{89-92}. Cr-spinel grains contain 8-10 wt% Al_2O_3, 11-13 wt% MgO, 18-24 wt% FeO, and 56-60 wt% Cr_2O_3 (Table 2).

Mineral zoning and overgrowths

A subset of the samples examined in the study (samples U1439C-2R3W 2-3, U1439C-15R1W 8-10, U1439C-19R2W 46-48, and U1439C-25R2W 18-19) showed prominent mineral zoning/overgrowth textures (these will be referred to as 2R3, 15R1, 19R2, and 25R2 for brevity). These samples were all from volcanic units in Hole U1439C, and encompass both HSB and LSB boninite subtypes (Reagan et al. 2015; 2017). These four samples contain olivine, enstatite, and clinoenstatite as phenocrysts in a groundmass dominated by acicular clinopyroxene (pigeonite to augite) in glass (Figure S.2).

Most of the larger pyroxene phenocrysts show calcic overgrowths ($En_{42\pm9}Fs_{14\pm4}Wo_{36\pm4.5}$) around enstatite cores ($En_{84\pm3}Fs_{12\pm0.6}Wo_{4\pm1}$) that are evident both optically and in electron backscatter imaging (Online Material[1] Table OM3 and Fig. OM2). Some of the larger enstatite grains and even a few of the large olivines appear to be nucleation sites for clinopyroxene. Large enstatite grains in samples 2R3 and 15R1 exhibit oscillatory zoning that is visible optically as well as via electron backscatter imaging. A subset of the calcic overgrowths exhibit anomalous enrichments in Al_2O_3 (typical pyroxenes ~4.0 wt%: anomalous overgrowths: up to 13.5 wt%), as well as high TiO_2 contents. When plotted on the pyroxene quadrilateral (Figure 3), the cores, standard rims/overgrowths, and aluminous overgrowths from samples 19R2 and 2R3 form three distinct clusters. Samples 15R1 and 25R2 differ from the other samples in this study as pyroxene compositions observed in these samples are more continuous from enstatite to augite (Figure 3, data can be found in Online Material[1] Table OM3 and OM4.). EPMA and ICP-TOF analyses revealed multiple zoning patterns. Small groundmass pyroxenes in sample 25R2 exhibit the most

235 complex zoning patterns with oscillatory, sector, and patchy zoning patterns appearing in many
236 of these crystals. Groundmass pyroxenes that show oscillatory zoning often contain magnesian
237 cores (i.e., Mg#: 80±5.5, Cr#: 25±4.1, and $Wo_{8\pm7.3}$) and calcic rims/overgrowths (i.e., Mg#:
238 50±10, Cr#: 1±2.8, and $Wo_{26\pm6.6}$); however, reverse zoning patterns have also been observed
239 (Figure S.3). Groundmass pyroxenes in samples 2R3, 15R1, and 19R2 exhibit patchy and sector
240 zoning with no evident oscillatory zoning. Some of the larger pyroxene grains in sample 15R1
241 show oscillatory zoning with minor changes in En and Fs components. Mn appears to be
242 following Fe in these oscillatory zoned pyroxenes. These larger pyroxenes also exhibit sector
243 zoning patterns with enriched Cr, Al, and Ti concentrations in sector zones (Figure 4). Large
244 pyroxene grains in sample 2R3 display oscillatory zoning with minor changes in En and Fs
245 components; however, sector zoning is not observed in this sample.
246 In sample 25R2, many olivine grains exhibit oscillatory zoning, with $Fo_{92\text{-}91}$ cores and
247 less magnesian $Fo_{90\text{-}86}$ rims (Online Material[1] Tabel OM5 and Fig. OM4). Sample 25R2 also
248 included multiple olivine grains with reverse oscillatory zoning, from $Fo_{88\text{-}87}$ cores to $Fo_{91\text{-}90}$
249 inner-rims, and then to $Fo_{88\text{-}87}$ outer rims (Online Material[1] Fig. OM4). Olivine zoning was not
250 observed in any samples other than 25R2.

251 ## DISCUSSION

252 ### Mineralogical and Mineral Chemistry Variations

253 The majority of the Expedition 352 boninite samples examined in this study and recent
254 studies (e.g., Whattam et al. 2020) exhibit phenocryst and matrix mineral compositions
255 consistent with fractional crystallization. The most common phenocryst assemblages
256 encountered are enstatite + olivine, sometimes enclosing Cr-spinel, with groundmass pigeonite
257 and, in some cases, late-forming augitic clinopyroxene. Plagioclase is only encountered as a

matrix phase in the highly differentiated high-Mg andesites/dacites, and always in association with augite. These assemblages are consistent with the progressive crystallization of magnesian boninite parental magmas, as has been documented by Umino (1986), Arculus et al. (1992), and Dobson et al. (2006).

However, a subset (~10%) of our samples, all at different stratigraphic levels, preserve phenocrysts and groundmass crystals that show complex zoning and overgrowth textures (Figure S.2). While both Umino (1986) and Dobson et al. (2006) report textural evidence for rapid crystallization (i.e., skeletal and feathery morphologies in microphenocrysts of clinopyroxene), neither study reports pyroxene overgrowth textures in their Chichijima boninite suites, or pyroxene compositions with Al_2O_3 or TiO_2 contents as high as those encountered in the Al-rich overgrowths in our Expedition 352 samples. The only study to report textures similar to those observed in this subset of boninite samples from Expedition 352 is Ohnenstetter and Brown (1992). The rocks examined in that study were recovered from a glassy boninite dike in New Caledonia and exhibit similar pyroxene zoning, overgrowth textures, and crystal morphologies. The key differences between the samples from that study and the samples from this study are: (1) the lack of olivine in the boninite dike, (2) oscillatory zoning in the boninite dike is only observed in microphenocrysts of orthopyroxene and skeletal clinoenstatite crystals, (3) the appearance of tschermakitic amphibole overgrowths on the pyroxene grains.

The Formation of Ca-Tschermak Pyroxenes

Late crystallizing clinopyroxene overgrowths are easily distinguished in those samples that include them by their brighter electron backscatter shading, and by their elevated Al and Ti contents. The overgrowths are similar compositionally to late crystallizing clinopyroxenes observed in experimental studies on quartz normative lunar basalts (Grove and Bence 1977) and

sudies of natural boninite samples (Ohnenstetter and Brown 1992; Dobson et al. 2006). These overgrowths are believed to develop due to the lack of Al-rich phases like plagioclase crystallizing prior to eruption. The melt thus becomes enriched in Al and Ti, which is then incorporated into the pyroxenes during rapid crystallization at high degrees of undercooling, similar to the way in which tschermakitic amphiboles are proposed to form in a New Caledonia boninite dike (i.e., Ohnenstetter and Brown 1992). It should also be noted that these pyroxene overgrowths often become more Al and Ti-rich towards the rim. This phenomenon is likely due to the rapid crystallization of pyroxene, depleting the crystal interface of compatible elements, and enriching it in incompatible and slow-diffusing elements like Al and Ti (Mollo et al. 2010, 2013). During this rapid crystallization process, Al substitutes into the tetrahedral site in place of Si, while Ti substitutes into the M1 site to charge balance the crystal (Ubide et al. 2019; Masotta et al. 2020). Whattam et al. (2020) suggests that Expedition 352 boninite melts ascended to the surface rapidly, as they appear to crystallize at similar temperatures to the fore-arc basalts recovered during Expedition 352, but at much lower pressures. Thus, the boninite melts ascended rapidly enough that they experienced little to no heat loss until they were near the surface, creating perfect conditions for crystallization driven by undercooling that resulted from decreases in pressure.

The fact that tschermakitic amphibole formed in a boninite dike from New Caledonia, but not in the Expedition 352 samples, is likely due to differences in the compositions of the dike and lavas. Sisson and Grove (1993) note that Na_2O in the melt must be ~4 wt% to stabilize amphibole in calc-alkaline andesites, so it is possible that the appearance of amphibole in the boninite dike may be related to increased Na_2O in the dike relative to the boninite lavas from this study. However; Ohnenstetter and Brown 1992 report Na_2O concentrations in glasses within the

304 boninite dike of 2.09 wt% in the glasses from the boninite dike which is nearly identical to the
305 Na_2O concentrations in glasses from the Expedition 352 boninite lavas (Coulthard et al. 2021),
306 so it seems unlikely that Na content is the controlling factor in this case. H_2O concentrations in
307 glass from the boninite dike are ~5.6 wt%, while concentraions in boninite glasses from
308 Expedition 352 lavas are ~1.32-3.21 wt% (Coulthard et al. 2021). It may be that these
309 comparatively lower H_2O concentrations inhibit amphibole crystallization in the Expedition 352
310 boninite melts.

311 **Pyroxene Zoning**

312 Pyroxenes can exhibit normal, reverse, sector, oscillatory, sector, or patchy zoning
313 depending on the magmatic conditions under which they form (Streck 2008). Normal zoning
314 refers to chemical variation that shifts from primitive to evolved in composition (i.e., Mg-rich to
315 Mg-poor in this study), while reverse zoning refers to the opposite of this pattern (i.e., Mg-poor
316 to Mg-rich). Normal and reverse zoning may alternate within a single crystal, forming bands that
317 are typically >10 μm wide. Oscillatory zoning refers to cases where the normal or reverse zoning
318 patterns repeat in an oscillating pattern. These oscillating zones can range in size, but are
319 typically ~1-3 μm in width, and in the case of this study exhibit abrupt compositional changes.
320 Sector zoning refers to crystals which contain chemical variations that correlate with different
321 crystallographic directions.

322 Normal zoning in pyroxenes is related to fractional crystallization of the parent melt or
323 high degrees of undercooling during crystallization (Shea and Hammer 2013; Benard et al.
324 2018), whereas reverse zoning is associated with reversals in magma composition (e.g., magma
325 mixing) or abrupt changes in crystallization conditions (Streck 2008; Saunders et al. 2012;
326 Petrone et al. 2016, 2018; Singer et al. 2016). Previous studies suggest that oscillatory zoning in

This is the peer-reviewed, final accepted version for American Mineralogist, published by the Mineralogical Society of America.
The published version is subject to change. Cite as Authors (Year) Title. American Mineralogist, in press.
DOI: https://doi.org/10.2138/am-2021-7733. http://www.minsocam.org/

pyroxenes can be driven by rapid crystallization and undercooling (Ohnenstetter and Brown 1992; Benard et al. 2018), based on plagioclase crystallization models (i.e., Ghiorso 1987; L'Heureux and Fowler 1996). In these models, less compatible elements (e.g., Cr, Al, Ti) are enriched near the crystal interface and then incorporated into the crystal as crystallization continues. This process repeats as more compatible elements (e.g., Mg, Ca) slowly**{{auth: okay?}}** diffuse toward the interface, and less compatible elements are incorporated into the crystal, resulting in oscillatory zoning. As well, other studies have contended that oscillatory zoning in pyroxenes may be related to magma mixing events (i.e., Petrone et al. 2016, 2018; Ubide and Kamber 2018; Ubide et al. 2019). In cases where boundary layer processes control oscillatory zoning, the zones are narrower (≈1-3 μm wide) and more numerous than what one would see in such features formed during magma mixing events (e.g., only a few oscillations, each ≈10-50 μm in thickness). Sector zoning in pyroxenes forms in response to modest degrees of undercooling (e.g., Shea and Hammer 2013; Ubide and Kamber 2018; Ubide et al. 2019; Masotta et al. 2020). Patchy zoning (i.e., zones which are not consistent with euhedral crystal growth) in pyroxenes has been related to changes in pressure, temperature, and H_2O content in the melt, as well as dissolution and recrystallization effects (Streck 2008; Crabtree and Lange 2010; Shea and Hammer 2013; Waters and Lange 2017).

Samples from this study contain examples of all of these pyroxene zoning patterns, indicating that they experienced a wide range of crystallization conditions during their formation. The appearance of groundmass pyroxenes with low-Ca cores and calcic overgrowths is likely related to rapid crystallization driven by undercooling upon ascent and eruption. As undercooling can be caused by changes in temperature or pressure, we suggest that the undercooling events that generated the calcic overgrowths were the result of decreases in pressure during ascent that

likely also changed the H_2O composition of the melt (e.g., Shea and Hammer 2013; Waters and Lange 2017). This process would have resulted in the rapid nucleation of pyroxene and the formation of patchy and sector zoning patterns observed in the groundmass pyroxenes studied.

Two of the samples from this study (2R3 and 15R1) contain zoned low-Ca pyroxene phenocrysts. Single-element maps of multiple pyroxene phenocrysts in sample 15R1 reveal complex sector and oscillatory zoning patterns, which vary from element to element. Some divalent cations (e.g., Mg, Fe, Mn) exhibit oscillatory zoning patterns while Al, Cr, and Ti exhibit sector zoning patterns (with some variation in the Cr zoning patterns) (Figures 4 & 6). Sector zoning of Al, Cr, and Ti has been observed in recent studies (i.e., Barnes et al. 2016; Ubide and Kamber 2018; Mao et al. 2019; Ubide et al. 2019; Masotta et al. 2020) and has been attributed the sluggish kinetic effects on pyroxene crystallization during moderate degrees of undercooling ($\Delta T<32$ ºC).

Chemical data from the sector zoned pyroxenes in this study revealed a positive correlation between Al, Cr, and Ti in most of the sector zones. Similar relationships are observed in undercooled boninite dikes from New Caledonia (Ohnenstetter and Brown 1992). Thus, it is likely that undercooling drove much of the crystallization in these low Ca pyroxenes, resulting in sector zoning due to the crystal kinetics, substitution, and charge balancing processes discussed in Ubide et al. (2019). However, correlations between the Mg/Fe and Cr/Al ratios in these crystals suggest that these pyroxene grains have experienced a more complex crystallization history than consistent undercooling. Elemental maps reveal that high Mg/Fe and Cr/Al oscillations are also correlated with Cr enriched and Al depleted zones, which cut across the sector zones (Figure 6). These oscillations suggest changes occurred in the magmatic system at multiple points in time, which led to interruptions in the growth of sector zoning, and enriched

the melt at the crystal interfaces with Mg and Cr. Based on observations from several previous studies (Petrone et al. 2016, 2018; Singer et al. 2016; Ubide and Kamber 2018; Ubide et al. 2019; Masotta et al. 2020), magma mixing between primitive and evolved boninite melt endmembers could cause an increase in temperature and enrich the melt in Mg and Cr (Figure 7).

Oscillatory zoning is also observed in some of the groundmass pyroxene grains from sample 25R2 (Figure 8). The acicular shape and small size (i.e., 50-100 μm) of these pyroxenes indicate that groundmass pyroxenes formed rapidly during an undercooling event. This indicates that oscillatory zoning in small pyroxenes may have been driven by rapid crystallization and undercooling, as suggested by Ohnenstetter and Brown (1992) and Benard et al. (2018). If this process were controlling the oscillatory zoning in sample 25R2, we would expect abundances of incompatible elements like Cr and Al to show a positive correlation. However, the opposite is observed: Cr follows Mg, and Al follows Fe and Ca (Figure 8). This kind of chemical relationship is what one would expect during mixing events, in which the crystals are interacting with multiple injections of magmas. Such patterns have been interpreted as mixing effects in both experimental and natural studies on pyroxene zoning (Ubide and Kamber 2018; Ubide et al. 2019; Masotta et al. 2020). So, some combination of undercooling and mixing processes are most likely affecting the crystallization of these groundmass pyroxenes.

Olivine Zoning and Xenocrysts

Olivine zoning usually appears as normal or reverse zoning in the Mg-Fe contents. However, oscillatory zoning can also be observed in minor elements (i.e., P, Al, and Cr) (Costa and Chakraborty 2004; Costa and Dungan 2005; Costa et al. 2008; Milman-Barris et al. 2008; Kahl et al. 2011, 2013; Shea et al. 2015a., 2015b., 2019). Olivine grains from this study are unusual in the way that they exhibit oscillatory zoning in both major (i.e., Mg and Fe) and minor

396 elements (i.e., Ca, Cr, Mn, and Ni) (Figure 5, S.4, & S.5). Our elemental maps reveal oscillatory
397 zoning patterns with respect to Fo content, which is also evident in the compositional transect
398 collected across this grain (Figure 5, S.4, & S.5).

399 Oscillatory zoning in olivine with respect to elements such as P, Al, and Cr is thought to
400 be caused by very rapid crystallization, which enriches the boundary layer in minor elements
401 because they are incompatible in olivine and slow diffusing (Milman-Barris et al. 2008; Shea et
402 al. 2015b, 2019). Shea et al. (2015b) suggest that a similar process might also cause oscillations
403 in the Fo content of olivine, which are subsequently lost due to the rapid re-equilibration of Mg
404 and Fe. However, if rapid crystallization was the cause for the Fo oscillations in the olivine
405 examined in this study, then Cr abundance patterns should correlate with those of Fe, Ca, and
406 Mn, instead of with more compatible and fast diffusing elements like Mg and Ni. It should also
407 be noted that Al zoning was not observed in any of the olivine grains from this study, further
408 supporting the hypothesis that this zoning was not caused by rapid crystallization (Figure 5).
409 Based on our geochemical observations, and other shipboard and post-cruise observations on
410 Expedition 352 samples (Reagan et al. 2015; 2017; see Insights from Petrography, Stratigraphy,
411 and Petrology below), we infer that the olivine zoning in this sample records magma mixing
412 events which episodically enriched the melts in Mg, Ni, and Cr.

413 The large, xenocrystic olivine observed in sample 25R2 likely came from a cumulate pile
414 within an evolving boninitic magmatic system (Figure S.4, Ol 6). That these xenocrysts have a
415 consistent composition of Fo_{88} suggests that they formed in equilibrium with a melt more
416 evolved than their current host. The smaller, zoned olivine in 25R2, with $Fo_{92\text{-}91}$ cores and rims
417 at ≈ Fo_{88}, were likely carried into the magma chamber in a more primitive boninite melt. Zoning
418 developed in these grains as a byproduct of this mixing event, resulting in rims that approach the

compositions of the xenocrysts. A similar process can also account for the reversely zoned olivine, which were likely growing suspended in the magma chamber or the cumulate pile, as reflected in their Fo_{88-87} cores. The rims of these olivines approach but never reach compositions as magnesian as olivine cores from the primitive boninite melt, due most likely to the hybridized composition of the mixed magma that they interacted with.

Magma Mixing

Mineral chemistry and mineral zoning patterns observed in this study indicate that boninite crystallization occurred in a dynamic and continuously evolving magmatic system. In this magmatic system, crystallization likely occurred as the magma ascended, and as the pressure and temperature decreased, leading to undercooling-driven crystallization. This process caused sector and patchy zoning in the groundmass pyroxenes, as well as the sector zoning patterns in the large low-Ca pyroxenes from 15R1. However, episodically this system experienced mafic (i.e., primitive boninite magma) recharge events, resulting in mixing between primitive and evolved magmas. These recharge events increased the temperature of the magma (i.e., decreasing the amount of undercooling) and enriched the evolving magma in key elements (e.g., Mg, Ni, Cr). These events led to the oscillatory zoning patterns observed in the large low-Ca pyroxenes from samples 15R1 and 2R3. Recharge events also caused normal, reverse, and oscillatory zoning in olivines, and resorption textures on the rims of olivine xenocrysts.

Zoning patterns created by mixing events are often used to determine the time between mixing events and eruptions. Mg-Fe diffusion across pyroxene and olivine zoning profiles has been used in other studies to place constraints on the time between mixing events and eruptions (Costa and Dungan 2005; Costa et al. 2008; Kahl et al. 2011, 2013; Saunders et al. 2012; Shea et al. 2015a., 2015b.; Petrone et al. 2016, 2018; Singer et al. 2016). Data from the transects

conducted in this study are not detailed enough to calculate reliable times; however, some inferences can be made based on the elements which show zoning in the olivines. Mg and Fe diffuse relatively fast in olivine (Costa and Chakraborty 2004; Costa et al. 2008; Shea et al. 2015a., 2015b) and are rapidly redistributed through crystals during solid-state re-equilibration with the evolving host magma. This high diffusivity is likely why the olivine xenocrysts do not exhibit zoning, as these crystals appear to have resided in a magma chamber for an extended period, and have thus re-equilibrated with the host magma. Thus, the presence of complex Mg-Fe oscillatory, normal, and reverse zoning in olivine phenocrysts, as we have found in this study, indicates that the events which produced them occurred shortly before eruption, before these crystals had time to re-equilibrate with the melt. Based on calculations of olivine residence time from previous studies, in which less complex zoning was observed in the olivine grains (i.e., Costa and Dungan 2005; Kahl et al. 2011, 2013; Shea et al. 2015a., 2015b), we suggest that the mixing events which led to these zoning features occurred within a couple of months to a couple of years before the eruption. While this hypothesis will require more detailed analyses of olivines to confirm, the likely short duration between mixing and eruption provides evidence that mafic recharge events may have driven the eruption of lavas through this section of the U1439C core.

Insights from Petrography, Stratigraphy, and Petrology

Shipboard portable X-ray fluorescence (PXRF) chemostratigraphic data (Ryan et al. 2017) document high chemical variability in specific horizons of the U1439C core that are suggestive of mingled or mixed melts; these trends are confirmed by shore-based XRF and ICPMS data (Shervais et al., 2021). These "mixing" horizons in the core show a reasonable alignment with the stratigraphic positions of the samples exhibiting anomalous mineral zoning (Figure S.6). Complex interactions among rising boninitic melts are also suggested by some of

the macro-scale fabrics found in the Hole U1439C and U1442A cores. Both cores preserve long (10 cm – 1 m scale) sections that demonstrate magma mingling fabrics, in which two different boninite melts are vertically intertwined, with visual evidence for interaction along with their margins (Reagan et al. 2015, 2017; Figure S.7; Shervais et al. 2021). As well, at the scale of standard thin sections, we see evidence for interaction, and incomplete mixing between more and less phenocryst-rich boninitic melts (e.g., Reagan et al. 2015, Figure S.8).

These observations, combined with the data from this study, indicate that magma mixing plays a significant role in the evolution of boninite magmas. The high chemical variability of some core sections observed in the chemostratigraphic data suggests that magmas at significantly different points in the fractionation process were present in the magma chamber and erupted together. Petrologic and chemical evidence from olivine and pyroxene indicate that mixing events occur within boninite magma bodies and, in some cases, may occur multiple times. The observation of macro- and microscale magma mingling interfaces, as well as preserved Fe-Mg oscillations in olivine grains, show that mixing events occured shortly before or during eruptions. Barometry from Whattam et al. (2020) indicates that crystallization in the Expedition 352 boninite melts occurred at pressures of ~0.2-0.4 kbar (i.e., 0.7-1.3 km).

We believe that this evidence shows that boninite magma bodies were located at shallow depths in the middle to the upper crust. Chemical zoning within these bodies, along with mixing events, could account for the chemical variability observed in the chemostratigraphy. These bodies include crystal cumulate piles that are overturned during mixing events, resulting in xenocryst crystal contamination (Figure 9).

IMPLICATIONS

Mineral zoning can be related to a variety of processes during crystal formation in magma chambers, and zoning patterns vary between minerals. However, a detailed analysis of mineral zoning patterns can be a powerful tool for understanding pre-eruptive magmatic processes. This study highlights the importance of multi-element chemical maps and chemical transects in studies of zoned minerals in igneous systems. This study and others cited here (e.g., Ubide et al. 2019), emphasize the usefulness of combining laser ablation techniques with traditional EPMA methods to allow us to interpret complex zoning patterns, which can vary between minerals and among elements. Observations from previous investigations indicate that the elemental patterns observed in this study were affected by a combination of undercooling and magma mixing processes. The use of edge-to-edge chemical transects alone, as is standard in many such studies, would have led to an oversimplified interpretation of the pre-eruptive history of the Expedition 352 boninite lavas.

This study also emphasizes the need to improve our understanding of elemental substitution into crystal lattices during different magmatic processes. Our work and that of previous zoning studies (see Pyroxene Zoning, and Olivine Zoning and Xenocrysts sections above for cited references) reveal that elemental substitutions are dependent on the conditions of the magmatic system, as well as the minerals into which the elements are substituting. This observation raises concerns as regards studies that attribute zoning to a specific process, solely based on observations in other mineral systems. Further experimental examinations, using elemental mapping methods, on various mineral systems at variable pressures, temperatures, and melt conditions are required to improve our understanding of elemental zoning. Such studies could further clarify the assignment of particular magmatic signatures to specific zoning patterns,

and increase the number of elements that may be used to interpret the pre-eruptive history of magmas.

A further implication of this study lies in the scientific benefits of conducting ostensibly education-focused investigations on scientifically significant suites of rock samples. The foundational petrographic and microprobe data for this investigation were collected over two years through the efforts of forty-nine University of South Florida undergraduate Geology majors, including three of this paper's authors, as part of an ongoing, multi-year course-based undergraduate research experience in co-author Ryan's junior-level GLY 3311C Mineralogy/Petrology/Geochemistry course. In these course-based activities, each student was tasked with completing a basic petrographic description (primary and secondary mineralogy, and textures) of one thin section and handsample from the Expedition 352 boninite suite, working largely in class during twice-weekly laboratory sessions. The course's laboratory fees pay for an hour of EPMA time per student, and ultimately the students, working in groups based on the depth horizons of their samples in the Site U1439 cores, selected those samples to be examined via microprobe based on their petrographic findings. EPMA measurements were largely conducted in the classroom by students under co-author Ryan's supervision, taking advantage of the remote operation capabilities of the Florida Center for Analytical Electron Microscopy EPMA system.

Having a large number of students spend an extended period of time microscopically examining Site U1439 boninite samples led to the recognition (by authors Scholpp, Hill, and Mack) of the small subset of samples that preserved anomalous mineral zoning and overgrowth features, features which have largely not been reported or highlighted in past studies of IBM boninites, including the recent study by Whattam et al. (2020) on these same cores. While

course-based undergraduate research experiences are predominantly touted for their educational benefits (see PCAST 2012; NAS 2015, 2017), there is also a real scientific value in bringing many sets of unbiased eyes to bear on complex igneous and metamorphic sample suites, such as may be recovered during IODP Expeditions.

Acknowledgments

Thanks go to Tom Beasley and postdoctoral fellows Sven Holbik and Chris Vidito for invaluable logistical support on the FCAEM EPMA and SEM systems, both for Ryan and all of the GLY 3311C students across several years. Thanks also go to Nick Bulloss for his assistance with the EPMA system at Boise State University. We also thank IODP for supporting an extended education-focused project with recovered Expedition 352 samples, and to the staff at the Kochi Core Repository for their creative aid in identifying suitable boninite samples for classroom petrographic and EPMA analysis. This project was supported by NSF grants OCE-1558855 and DUE-1323275 to Jeff Ryan and OCE-1558689 to Shervais.

References

Arculus, R.J., Pearce, J.A., Murton, B.J., and Van der Laan, S.R. (1992) Igneous stratigraphy and major element geochemistry of Holes 786A and 786B. In Proceedings of the Ocean Drilling Program, Scientific Results Vol. 125, pp. 143–169. Ocean Drilling Program, College Station, TX.

Barnes, S.J., Mole, D.R., Le Vaillant, M., Campbell, M.J., Verrall, M.R., Roberts, M.P., and Evans, N.J. (2016) Poikilitic Textures, Heteradcumulates and Zoned Orthopyroxenes in the Ntaka Ultramafic Complex, Tanzania: Implications for Crystallization Mechanisms of Oikocrysts. Journal of Petrology, 57, 1171–1198.

Bédard, J.H., Lauzière, K., Tremblay, A., and Sangster, A. (1998) Evidence for forearc seafloor-spreading from the Betts Cove ophiolite, Newfoundland: oceanic crust of boninitic affinity. Tectonophysics, 284, 233–245.

Bénard, A., Nebel, O., Ionov, D.A., Arculus, R.J., Shimizu, N., and Métrich, N. (2016) Primary silica-rich picrite and high-Ca boninite melt inclusions in pyroxenite veins from the Kamchatka sub-arc mantle. Journal of Petrology, 57, 1955–1982.

Bloomer, S.H. (1979) Mariana arc-trench studies: Petrology of boninites and evidence for a" boninite series". EOS (Amer. Geophys. Union Trans.), 60, 968.

562 Bloomer, S.H., and Hawkins, J.W. (1987) Petrology and geochemistry of boninite series
563 volcanic rocks from the Mariana trench. Contributions to Mineralogy and Petrology, 97,
564 361–377.

565 Cameron, W.E. (1985) Petrology and origin of primitive lavas from the Troodos ophiolite,
566 Cyprus. Contributions to Mineralogy and Petrology, 89, 239–255.

567 Cameron, W.E., McCulloch, M.T., and Walker, D.A. (1983) Boninite petrogenesis: Chemical
568 and Nd-Sr isotopic constraints. Earth and Planetary Science Letters, 65, 75–89.

569 Costa, F., and Chakraborty, S. (2004) Decadal time gaps between mafic intrusion and silicic
570 eruption obtained from chemical zoning patterns in olivine. Earth and Planetary Science
571 Letters, 227, 517–530.

572 Costa, F., and Dungan, M. (2005) Short time scales of magmatic assimilation from diffusion
573 modeling of multiple elements in olivine. Geology, 33, 837–840.

574 Costa, F., Dohmen, R., and Chakraborty, S. (2008) Time Scales of Magmatic Processes from
575 Modeling the Zoning Patterns of Crystals. Reviews in Mineralogy and Geochemistry, 69,
576 545–594.

577 Coulthard Jr, D.A., Reagan, M.K., Shimizu, K., Bindeman, I.N., Brounce, M., Almeev, R.R.,
578 Ryan, J., Chapman, T., Shervais, J., and Pearce, J.A. (2021) Magma Source Evolution
579 Following Subduction Initiation: Evidence From the Element Concentrations, Stable Isotope
580 Ratios, and Water Contents of Volcanic Glasses From the Bonin Forearc (IODP Expedition
581 352). Geochemistry, Geophysics, Geosystems, 22, e2020GC009054.

582 Crabtree, S.M., and Lange, R.A. (2010) Complex Phenocryst Textures and Zoning Patterns in
583 Andesites and Dacites: Evidence of Degassing-Induced Rapid Crystallization? Journal of
584 Petrology, 52, 3–38.

585 Crawford, A.J., Falloon, T.J., and Green, D.H. (1989) Classification, petrogenesis and tectonic
586 setting of boninites.

587 De Campos, C.P., Perugini, D., Ertel-Ingrisch, W., Dingwell, D.B., and Poli, G. (2011)
588 Enhancement of magma mixing efficiency by chaotic dynamics: an experimental study.
589 Contributions to Mineralogy and Petrology, 161, 863–881.

590 Dietrich, V., Emmermann, R., Oberhänsli, R., and Puchelt, H. (1978) Geochemistry of basaltic
591 and gabbroic rocks from the West Mariana basin and the Mariana trench. Earth and
592 Planetary Science Letters, 39, 127–144.

593 Dobson, P.F., Blank, J.G., Maruyama, S., and Liou, J.G. (2006) Petrology and geochemistry of
594 boninite-series volcanic rocks, Chichi-Jima, Bonin Islands, Japan. International Geology
595 Review, 48, 669–701.

596 Druitt, T.H., Costa, F., Deloule, E., Dungan, M., and Scaillet, B. (2012) Decadal to monthly
597 timescales of magma transfer and reservoir growth at a caldera volcano. Nature, 482, 77.

598 Expedition 352 Scientists (2014) International Ocean Discovery Program Expedition 352
599 Preliminary Report: Testing subduction initiation and ophiolite models by drilling the outer
600 Izu-Bonin Mariana fore arc. International Ocean Discovery Program, 352.

601 Falloon, T.J., and Crawford, A.J. (1991) The petrogenesis of high-calcium boninite lavas
602 dredged from the northern Tonga ridge. Earth and Planetary Science Letters, 102, 375–394.

603 Falloon, T.J., Malahoff, A., Zonenshaina, L.P., and Bogdanova, Y. (1992) Petrology and
604 geochemistry of back-arc basin basalts from Lau Basin spreading ridges at 15, 18 and 19 S.
605 Mineralogy and Petrology, 47, 1–35.

606 Ghiorso, M.S. (1987) Chemical mass transfer in magmatic processes. 3. Crystal growths,
607 chemical diffusion and thermal diffusion in multicomponent silicate melts. Contributions to
608 Mineralogy and Petrology, 96, 291–313.

609 Grove, T.L., and Bence, A.E. (1977) Experimental study of pyroxene-liquid interaction in
610 quartz-normative basalt 15597. In Lunar and Planetary Science Conference Proceedings
611 Vol. 8, pp. 1549–1579.

612 Hickey, R.L., and Frey, F.A. (1982) Geochemical characteristics of boninite series volcanics:
613 implications for their source. Geochimica et Cosmochimica Acta, 46, 2099–2115.

614 Humphreys, M.C.S., Christopher, T., and Hards, V. (2009) Microlite transfer by disaggregation
615 of mafic inclusions following magma mixing at Soufrière Hills volcano, Montserrat.
616 Contributions to Mineralogy and Petrology, 157, 609–624.

617 Ishikawa, T., Umino, S., and Kazuya, N. (2002) Boninitic volcanism in the Oman ophiolite:
618 Implications for thermal condition during transition from spreading ridge to arc. Geology,
619 30, 899–902.

620 Ishikawa, T., Fujisawa, S., Nagaishi, K., and Masuda, T. (2005) Trace element characteristics of
621 the fluid liberated from amphibolite-facies slab: Inference from the metamorphic sole
622 beneath the Oman ophiolite and implication for boninite genesis. Earth and Planetary
623 Science Letters, 240, 355–377.

624 Ishizuka, O., Taylor, R.N., Yuasa, M., and Ohara, Y. (2011) Making and breaking an island arc:
625 A new perspective from the Oligocene Kyushu-Palau arc, Philippine Sea. Geochemistry,
626 Geophysics, Geosystems, 12.

627 Johanssen, A. (1937) A descriptive petrography of the igneous rocks: The intermediate rocks.
628 University of Chicago Press, 3.

629 Kahl, M., Chakraborty, S., Costa, F., and Pompilio, M. (2011) Dynamic plumbing system
630 beneath volcanoes revealed by kinetic modeling, and the connection to monitoring data: An
631 example from Mt. Etna. Earth and Planetary Science Letters, 308, 11–22.

632 Kahl, M., Chakraborty, S., Costa, F., Pompilio, M., Liuzzo, M., and Viccaro, M. (2013)
633 Compositionally zoned crystals and real-time degassing data reveal changes in magma
634 transfer dynamics during the 2006 summit eruptive episodes of Mt. Etna. Bulletin of
635 Volcanology, 75, 692.

636 Kanayama, K., Umino, S., and Ishizuka, O. (2012) Eocene volcanism during the incipient stage
637 of Izu–Ogasawara Arc: Geology and petrology of the Mukojima Island Group, the
638 Ogasawara Islands. Island Arc, 21, 288–316.

639 Kanayama, K., Kitamura, K., and Umino, S. (2013) New geochemical classification of global
640 boninites. IAVCEI 2013 Scientific Assembly Abstracts.

641 Kelemen, P.B., Johnson, K.T.M., Kinzler, R.J., and Irving, A.J. (1990) High-field-strength
642 element depletions in arc basalts due to mantle–magma interaction. Nature, 345, 521–524.

643 Klemme, S., Blundy, J.D., and Wood, B.J. (2002) Experimental constraints on major and trace
644 element partitioning during partial melting of eclogite. Geochimica et Cosmochimica Acta,
645 66, 3109–3123.

646 Kuroda, N., and Shiraki, K. (1975) Boninite and related rocks of Chichi-jima, Bonin Islands,
647 Japan. Rep. Fac. Sci. Shizuoka Univ., 10, 145–155.

648 Kyser, T.K., Cameron, W.E., and Nisbet, E.G. (1986) Boninite petrogenesis and alteration
649 history: constraints from stable isotope compositions of boninites from Cape Vogel, New
650 Caledonia and Cyprus. Contributions to Mineralogy and Petrology, 93, 222–226.

651 L'Heureux, I., and Fowler, A.D. (1996) Isothermal constitutive undercooling as a model for
652 oscillatory zoning in plagioclase. The Canadian Mineralogist, 34, 1137–1147.

653 Li, H.-Y., Taylor, R.N., Prytulak, J., Kirchenbaur, M., Shervais, J.W., Ryan, J.G., Godard, M.,
654 Reagan, M.K., and Pearce, J.A. (2019) Radiogenic isotopes document the start of
655 subduction in the Western Pacific. Earth and Planetary Science Letters, 518, 197–210.

656 Li, Y.-B., Kimura, J.-I., Machida, S., Ishii, T., Ishiwatari, A., Maruyama, S., Qiu, H.-N.,
657 Ishikawa, T., Kato, Y., Haraguchi, S., and others (2013) High-Mg Adakite and Low-Ca
658 Boninite from a Bonin Fore-arc Seamount: Implications for the Reaction between Slab
659 Melts and Depleted Mantle. Journal of Petrology, 54, 1149–1175.

660 Mao, Y.-J., Barnes, S.J., Qin, K.-Z., Tang, D., Martin, L., Su, B., and Evans, N.J. (2019) Rapid
661 orthopyroxene growth induced by silica assimilation: constraints from sector-zoned
662 orthopyroxene, olivine oxygen isotopes and trace element variations in the Huangshanxi Ni–
663 Cu deposit, Northwest China. Contributions to Mineralogy and Petrology, 174, 33.

664 Masotta, M., Pontesilli, A., Mollo, S., Armienti, P., Ubide, T., Nazzari, M., and Scarlato, P.
665 (2020) The role of undercooling during clinopyroxene growth in trachybasaltic magmas:
666 Insights on magma decompression and cooling at Mt. Etna volcano. Geochimica et
667 Cosmochimica Acta, 268, 258–276.

668 Meffre, S., Falloon, T.J., Crawford, T.J., Hoernle, K., Hauff, F., Duncan, R.A., Bloomer, S.H.,
669 and Wright, D.J. (2012) Basalts erupted along the Tongan fore arc during subduction
670 initiation: Evidence from geochronology of dredged rocks from the Tonga fore arc and
671 trench. Geochemistry, Geophysics, Geosystems, 13.

672 Meijer, A. (1980) Primitive Arc Volcanism and a Boninite Series: Examples from Western
673 Pacific Island Arcs. In The Tectonic and Geologic Evolution of Southeast Asian Seas and
674 Islands pp. 269–282. American Geophysical Union (AGU).

675 Meijer, A., Anthony, E., and Reagan, M. (1982) Petrology of volcanic-rocks from the fore-arc
676 sites. Initial Reports of the Deep Sea Drilling Project, 60, 709–729.

677 Milman-Barris, M.S., Beckett, J.R., Baker, M.B., Hofmann, A.E., Morgan, Z., Crowley, M.R.,
678 Vielzeuf, D., and Stolper, E. (2008) Zoning of phosphorus in igneous olivine. Contributions
679 to Mineralogy and Petrology, 155, 739–765.

680 Mollo, S., Del Gaudio, P., Ventura, G., Iezzi, G., and Scarlato, P. (2010) Dependence of
681 clinopyroxene composition on cooling rate in basaltic magmas: Implications for
682 thermobarometry. Lithos, 118, 302–312.

683 Mollo, S., Putirka, K., Misiti, V., Soligo, M., and Scarlato, P. (2013) A new test for equilibrium
684 based on clinopyroxene–melt pairs: Clues on the solidification temperatures of Etnean
685 alkaline melts at post-eruptive conditions. Chemical Geology, 352, 92–100.

686 Murton, B.J., Peate, D.W., Arculus, R.J., Pearce, J.A., and Van der Laan, S. (1992) Trace-
687 element geochemistry of volcanic rocks from site 786: The Izu-Bonin Forearc. Proceedings
688 of the Ocean Drilling Program Scientific Results, 125, 211–235.

689 National Academies of Sciences, Engineering, and Medicine (2015) Integrating Discovery-
690 Based Research into the Undergraduate Curriculum: Report of a Convocation. Washington,
691 DC: National Academies Press, https://doi.org/10.17226/21851.

692 National Academies of Sciences, Engineering, and Medicine (2017) Undergraduate Research
693 Experiences for STEM Students: Successes, Challenges, and Opportunities. Washington,
694 DC: The National Academies Press. doi: https://doi.org/10.17226/24622.

695 Ohnenstetter, D., and Brown, W.L. (1992) Overgrowth Textures, Disequilibrium Zoning, and
696 Cooling History of a Glassy Four-Pyroxene Boninite Dyke from New Caledonia. Journal of
697 Petrology, 33, 231–271.

698 Pagé, P., Bédard, J.H., Schroetter, J.-M., and Tremblay, A. (2008) Mantle petrology and
699 mineralogy of the Thetford Mines Ophiolite Complex. Links Between Ophiolites and LIPs
700 in Earth History, 100, 255–292.

701 Pagé, P., Bédard, J.H., and Tremblay, A. (2009) Geochemical variations in a depleted fore-arc
702 mantle: The Ordovician Thetford Mines Ophiolite. Mantle Dynamics and Crust-Mantle
703 Interactions in Collisional Orogens, 113, 21–47.

704 Pearce, J.A., and Reagan, M.K. (2019) Identification, classification, and interpretation of
705 boninites from Anthropocene to Eoarchean using Si-Mg-Ti systematics. Geosphere, 15,
706 1008–1037.

707 Pearce, J.A., van der Laan, S.R., Arculus, R.J., Murton, B.J., Ishii, T., Peate, D.W., and
708 Parkinson, I.J. (1992) Boninite and harzburgite from Leg 125 (Bonin-Mariana forearc): A
709 case study of magma genesis during the initial stages of subduction. In Proceedings of the
710 ocean drilling program, scientific results Vol. 125, pp. 623–659. Citeseer.

711 Pearce, J.A., Kempton, P.D., Nowell, G.M., and Noble, S.R. (1999) Hf-Nd element and isotope
712 perspective on the nature and provenance of mantle and subduction components in Western
713 Pacific arc-basin systems. Journal of Petrology, 40, 1579–1611.

714 Petrone, C.M., Bugatti, G., Braschi, E., and Tommasini, S. (2016) Pre-eruptive magmatic
715 processes re-timed using a non-isothermal approach to magma chamber dynamics. Nature
716 Communications, 7, 12946.

717 Petrone, C.M., Braschi, E., Francalanci, L., Casalini, M., and Tommasini, S. (2018) Rapid
718 mixing and short storage timescale in the magma dynamics of a steady-state volcano. Earth
719 and Planetary Science Letters, 492, 206–221.

720 Presidents Council of Advisor on Science and Technology (2012) Report to the President.
721 Engage to Excel: Producing One Million Additional College Graduates with Degrees in
722 Science, Technology, Engineering and Mathematics. 103 p.

723 Reagan, M.K., Ishizuka, O., Stern, R.J., Kelley, K.A., Ohara, Y., Blichert-Toft, J., Bloomer,
724 S.H., Cash, J., Fryer, P., Hanan, B.B., and others (2010) Fore-arc basalts and subduction
725 initiation in the Izu-Bonin-Mariana system. Geochemistry, Geophysics, Geosystems, 11.

726 Reagan, M.K., Pearce, J.A., Petronotis, K., and Expedition 352 Scientists (2015) Expedition 352
727 summary. Proceedings of the International Ocean Discovery Program, 352, 1–32.

728 Reagan, M.K., Pearce, J.A., Petronotis, K., Almeev, R.R., Avery, A.J., Carvallo, C., Chapman,
729 T., Christeson, G.L., Ferré, E.C., Godard, M., and others (2017) Subduction initiation and
730 ophiolite crust: new insights from IODP drilling. International Geology Review, 59, 1439–
731 1450.

732 Reagan, M.K., Heaton, D.E., Schmitz, M.D., Pearce, J.A., Shervais, J.W., and Koppers, A.A.P.
733 (2019) Forearc ages reveal extensive short-lived and rapid seafloor spreading following
734 subduction initiation. Earth and Planetary Science Letters, 506, 520–529.

735 Resing, J.A., Rubin, K.H., Embley, R.W., Lupton, J.E., Baker, E.T., Dziak, R.P., Baumberger,
736 T., Lilley, M.D., Huber, J.A., Shank, T.M., and others (2011) Active submarine eruption of
737 boninite in the northeastern Lau Basin. Nature Geoscience, 4, 799.

738 Rossi, S., Petrelli, M., Morgavi, D., Vetere, F.P., Almeev, R.R., Astbury, R.L., and Perugini, D.
739 (2019) Role of magma mixing in the pre-eruptive dynamics of the Aeolian Islands
740 volcanoes (Southern Tyrrhenian Sea, Italy). Lithos, 324–325, 165–179.

741 Ryan, J.G. (2013) Embedding research practice activities into earth and planetary science
742 courses through the use of remotely operable analytical instrumentation: Interventions and
743 impacts on student perceptions and activities. Geoscience Research and Education:
744 Teaching at Universities. New York: Springer Verlag, 149–162.

745 Ryan, J.G., Shervais, J.W., Li, Y., Reagan, M.K., Li, H.Y., Heaton, D., Godard, M.,
746 Kirchenbaur, M., Whattam, S.A., and Pearce, J.A. (2017) Application of a handheld X-ray
747 fluorescence spectrometer for real-time, high-density quantitative analysis of drilled igneous
748 rocks and sediments during IODP Expedition 352. Chemical Geology, 451, 55–66.

749 Saunders, K., Rinnen, S., Blundy, J., Dohmen, R., Klemme, S., and Arlinghaus, H.F. (2012)
750 TOF-SIMS and electron microprobe investigations of zoned magmatic orthopyroxenes:
751 First results of trace and minor element analysis with implications for diffusion modeling.
752 American Mineralogist, 97, 532–542.

753 Shea, T., and Hammer, J.E. (2013) Kinetics of cooling- and decompression-induced
754 crystallization in hydrous mafic-intermediate magmas. Journal of Volcanology and
755 Geothermal Research, 260, 127–145.

756 Shea, T., Costa, F., Krimer, D., and Hammer, J.E. (2015a) Accuracy of timescales retrieved from
757 diffusion modeling in olivine: A 3D perspective†. American Mineralogist, 100, 2026–2042.

758 Shea, T., Lynn, K.J., and Garcia, M.O. (2015b) Cracking the olivine zoning code: Distinguishing
759 between crystal growth and diffusion. Geology, 43, 935–938.

760 Shea, T., Hammer, J.E., Hellebrand, E., Mourey, A.J., Costa, F., First, E.C., Lynn, K.J., and
761 Melnik, O. (2019) Phosphorus and aluminum zoning in olivine: contrasting behavior of two
762 nominally incompatible trace elements. Contributions to Mineralogy and Petrology, 174, 85.

763 Shervais, J.W., Reagan, M., Haugen, E., Almeev, R.R., Pearce, J.A., Prytulak, J., Ryan, J.G.,
764 Whattam, S.A., Godard, M., Chapman, T., Li, H-Y., Nelson, W., Kirchenbaur, M., Heaton,
765 D., Kurz, W., Shimizu, K., Sakuyama, T., Li, Y., and Vetter, S.K. (2019) Magmatic
766 Response to Subduction Initiation: Part 1. Fore-arc Basalts of the Izu-Bonin Arc From IODP
767 Expedition 352. Geochemistry, Geophysics, Geosystems, 20, 314–338.

768 Shervais, J., Reagan, M., Godard, M., Prytulak, J., Ryan, J.G., Pearce, J., Almeev, R., Li, H.-Y. ,
769 Haugen, E., Chapman, T., Kurz, W., Nelson, W., Heaton, D., Kirchenbaur, M., Shimizu, K.,
770 Sakuyama, T., Vetter, S., Li, Y. and Whattam, S. (2021) Magmatic response to subduction
771 initiation part II: Boninites and releated rocks of the Izu-Bonin Arc from IODP Expedition
772 352. Geochemistry Geophysics Geosystems, 22, e2020GC009093.
773 https://doi.org/10.1029/2020GC009093.

774 Singer, B.S., Costa, F., Herrin, J.S., Hildreth, W., and Fierstein, J. (2016) The timing of
775 compositionally-zoned magma reservoirs and mafic 'priming' weeks before the 1912
776 Novarupta-Katmai rhyolite eruption. Earth and Planetary Science Letters, 451, 125–137.

777 Sisson, T.W., and Grove, T.L. (1993) Experimental investigations of the role of H 2 O in calc-
778 alkaline differentiation and subduction zone magmatism. Contributions to mineralogy and
779 petrology, 113, 143–166.

780 Sisson, T.W., and Bronto, S. (1998) Evidence for pressure-release melting beneath magmatic
781 arcs from basalt at Galunggung, Indonesia. Nature, 391, 883–886.

782 Sparks, S.R.J., Sigurdsson, H., and Wilson, L. (1977) Magma mixing: a mechanism for
783 triggering acid explosive eruptions. Nature, 267, 315–318.

784 Stern, R.J., and Bloomer, S.H. (1992) Subduction zone infancy: Examples from the Eocene Izu-
785 Bonin-Mariana and Jurassic California arcs. GSA Bulletin, 104, 1621–1636.

786 Streck, M.J. (2008) Mineral Textures and Zoning as Evidence for Open System Processes.
787 Reviews in Mineralogy and Geochemistry, 69, 595–622.

788 Taylor, R.N., Nesbitt, R.W., Vidal, P., Harmon, R.S., Auvray, B., and Croudace, I.W. (1994)
789 Mineralogy, Chemistry, and Genesis of the Boninite Series Volcanics, Chichijima, Bonin
790 Islands, Japan. Journal of Petrology, 35, 577–617.

791 Ubide, T., and Kamber, B.S. (2018) Volcanic crystals as time capsules of eruption history.
792 Nature Communications, 9, 326.

793 Ubide, T., Mollo, S., Zhao, J., Nazzari, M., and Scarlato, P. (2019) Sector-zoned clinopyroxene
794 as a recorder of magma history, eruption triggers, and ascent rates. Geochimica et
795 Cosmochimica Acta, 251, 265–283.

796 Umino, S. (1986) Magma mixing in boninite sequence of Chichijima, Bonin Islands. Journal of
797 Volcanology and Geothermal Research, 29, 125–157.

798 Van Malderen, S. (2017) Optimization of methods based on laser ablation-ICP-mass
799 spectrometry (LA-ICP-MS) for 2-D and 3-D elemental mapping. PhD Thesis, Ghent
800 University.

Van Malderen, S.J., Van Acker, T., and Vanhaecke, F. (2020) Sub-micrometer Nanosecond LA-ICP-MS Imaging at Pixel Acquisition Rates above 250 Hz via a Low-Dispersion Setup. Analytical Chemistry, 92, 5756–5764.

Waters, L.E., and Lange, R.A. (2017) An experimental study of (Fe-Mg) KD between orthopyroxene and rhyolite: a strong dependence on H2O in the melt. Contributions to Mineralogy and Petrology, 172, 42.

Whattam, S.A., Shervais, J.W., Reagan, M.K., Coulthard JR, D.A., Pearce, J.A., Jones, P., Seo, J., Putirka, K., Chapman, T., Heaton, D., and others (2020) Mineral compositions and thermobarometry of basalts and boninites recovered during IODP Expedition 352 to the Bonin forearc. American Mineralogist, 105, 1490–1507.

Wyman, D.A. (1999) Paleoproterozoic boninites in an ophiolite-like setting, Trans-Hudson orogen, Canada. Geology, 27, 455–458.

List of Figure Captions

Figure 1

Drillsite map and theorectical crosssection of the IBM forearc. (a) Location of drill-sites U1439, U1440, U1441, U1442 in relation to the Bonin Islands (e.g., Chichijima) on the Ogasawara Plateau. (b) Theoretical cross section of the forearc, showing the location of the drill sites for IODP Expedition 352 (modified from Reagan et al. 2015).

Figure 2

Core summary from hole U1439C and U1442A based on Reagan et al. (2015). Red Arrows to the left of the U1439C stratigraphic section, point to the core section which samples U1439C-2R3W 2-3, U1439C-15R1W 8-10, U1439C-19R2W 46-48, and U1439C-25R2W 18-19 came from. Zones indicating mixed magmas on the stratigraphic sections were identified by the shipboard crew.

Figure 3

Pyroxene Quadrilateral with pyroxenes from samples samples U1439C-2R3W 2-3 (2R3), U1439C-15R1W 8-10 (15R1), U1439C-19R2W 46-48 (19R2), and U1439C-25R2W 18-19 (25R2) plotted. Enstatite (En), Wollastonite (Wo), Ferrosilite (Fs), and Ca-Tschermak (CaTs).

Pyroxenes that have anomalous Al concentration show a trend towards ferrosilite and can be seen in the brown dashed circle. Data can be found in Online Material[1] Table OM3 and OM4.

Figure 4

Elemental maps of low-Ca pyroxene phenocrysts from sample 15R1. Red arrows in elemental maps point to zones enriched in Mg & Cr and depleted in Fe, Al, Mn, and Ti. Labels (Px 1) and (Px 2) in map (a) refer to the label used in (Online Material[1] Table OM3.) and (Figs. 6 and Online Material[1] Table OM3) to identify the individual pyroxene grains. Label (UPx) in map (a) refers to the label used in (Fig. 6) as an across grain chemical transect was not made for this pyroxene grain. Unanalyzed Pyroxene (UPx). Elemental maps were produced using LA-ICP-TOF.

Figure 5

Elemental maps of zoned olivine phenocrysts from sample 25R1. Red arrows in elemental maps point to zones enriched in Mg, Cr, and Ni and depleted in Fe, Mn, and Ca. White arrows on maps (b), (e), and (g.) points at a zone between the core and rim of this grain, which is more depleted in Mg, Ni, and Cr than the rim of the grain. Label (Ol 1) in the bottom left-hand corner of map (a) refers to the label used in (Online Material[1] Table OM5) and (Online Material[1] Fig. OM4) to identify the individual olivine grains. Elemental maps (a), (b), (c), and (d) were produced using EPMA. Elemental maps (e), (f.), (g.), and (h.) were generated using LA-ICP-TOF.

Figure 6

Drawn models of the zoning patterns observed in low-Ca pyroxene phenocrysts from sample 15R1 (shown in Fig. 4). Drawings in the first column highlight the oscillatory zoning patterns observed in Mg and Cr. Drawings in the second column highlight the sector zoning pattern observed in Cr, Al, and Ti. Drawings in the last column combine the zoning profiles so they can

be compared with each other. Labels (Px 1) and (Px 2) refer to the labels used in Online Material[1] Table OM3, Figure 4, and Figure OM3 to identify the individual pyroxene grains. Label (UPx) refers to the label used in Figure 4 as an across grain chemical transect was not made for this pyroxene grain. Unanalyzed Pyroxene (UPx).

Figure 7

Idealized crystallization model for the development of complex pyroxene zoning patterns observed in this study. (a) Idealized pyroxene crystallization history showing the development of the sector and oscillatory zoning profiles as the crystal grows in an open igneous system. Progression from core to rim is indicated above the models. Crystal shape and sector zones based on the 2D model in (b) (b) Hypothetical 2D model of the crystal of a pyroxene crystal (cutting through the center of the crystal) revealing the sector zoning pattern along the a- and c- axis (the {-111} and {100} prism forms). Modified from Ubide et al. (2019). Note this model is not meant to show the exact zoning profiles observed in pyroxenes from sample 15R1 (Fig. 4) as we do not know the exact angle in which those crystals were cut and polished during sample preparation. This model is only meant to show what the zoning profile would look like in a perfectly cut crystal, based on the hypothesized open-system processes from this paper.

Figure 8

BSE image and elemental maps of zoned groundmass clinopyroxene from sample 25R1. The red box in the BSE image (a) shows the area which was analyzed in elemental maps (b), (c), (d), (e), and (f). Red Arrows in the elemental maps point to Mg & Cr enriched zones in the pyroxene. Blue arrows in the elemental maps point to Mg, Fe, and Cr rich core of the grain, which is depleted in Ca and Al. Green arrow in elemental map (c) points to Fe enrichment around the edge of the grain. Label (Px 14) in the top right-hand corner of map (a) refers to the label used in

(Online Material[1] Table OM3) and (Online Material[1] Figure OM3) to identify the individual pyroxene grains.

Figure 9

Boninite magma chamber and mixing model. Primitive boninite melts pond beneath the fore-arc crust before ascending through a crystal mush zone (a) Primitive melts begin to crystallize as they migrate through the crystal mush, ascending towards a fractionating magma chamber with a cumulate pile (b). Primitive melts enter the chamber and dislodging cumulate material (c). Primitive plume ascends into the evolved magma chamber resulting in magma mixing, along with reverse and normal zoning patterns (c).

Tables

Table 1. Typical Magma End-member Assembleges.

End member	Phenocrysts	Minor minerals	Matrix
HSB	Orthopyroxene ± Olivine	Cr-spinel	Clinopyroxene
LSB	Olivine + Orthopyroxene	Cr-spinel	Clinopyroxene ± Plagioclase
HMA	Plagioclase + Clinopyroxene	Magnetite + Ilmenite	Clinopyroxene + Plagioclase

[a] End-members: High-Si Boninite (HSB), Low-Si Boninite (LSB), High-Mg Andesite (HMA)

Table 2. Normal Mineral Composition Observed in Magma Endmembers (Non-Mixing Samples).

Sample	Mineral	SiO2 (wt%)	TiO2 (wt%)	Al2O3 (wt%)	Cr2O3 (wt%)	FeO (wt%)	MgO (wt%)	MnO (wt%)	NiO (wt%)	CaO (wt%)	Na2O (wt%
U1439A-21X-1-W 2-3	En	57.18	0.00	0.67	0.42	7.70	32.33	0.07	0.07	1.24	0.04
U1439A-21X-1-W 2-3	En	56.44	0.00	1.19	0.61	8.74	31.68	0.09	0.10	1.54	0.02

U1439A-21X-1-W 2-3	CLEN	55.51	0.00	2.10	0.31	10.56	27.90	0.11	0.08	4.27	0.05
U1439A-21X-1-W 2-3	PIG	52.64	0.36	4.02	0.19	10.87	22.72	0.11	0.08	9.85	0.09
U1439A-21X-1-W 2-3	Cr-Sp	0.31	0.02	8.62	60.14	19.33	10.54	0.16	0.14	0.04	0.00
U1439A-21X-1-W 2-3	Cr-Sp	0.12	0.13	8.40	58.16	23.62	11.13	0.18	0.13	0.06	0.05
U1439C-33R-1-W, 137-140	Cr-Sp	0.13	0.08	9.71	56.72	19.36	13.48	0.30	0.00	0.12	0.09
U1439C-33R-1-W, 137-140	Ol	39.72	0.00	0.07	0.08	8.51	52.41	0.14	0.00	0.15	0.02
U1439C-29R-2-W 93-94	AUG	50.59	0.15	2.69	0.96	3.92	18.38	0.14	0.00	23.16	0.17
U1439C-29R-2-W 93-94	AUG	50.13	0.00	2.13	0.60	3.87	20.51	0.13	0.00	23.00	0.20
U1439C-34G-1-W 45-46	Ol	41.42	0.00	0.00	0.12	8.87	50.06	0.05	0.40	0.14	0.00
U1439C-34G-1-W 45-46	AUG	49.72	0.44	6.85	0.09	8.40	15.33	0.06	0.02	18.15	0.17
U1439C-34G-1-W 45-46	CLEN	56.03	0.00	1.40	0.76	8.90	29.19	0.10	0.04	3.59	0.04
U1439C-34G-1-W 45-46	CLEN	56.31	0.00	1.29	0.49	8.51	30.45	0.12	0.04	2.81	0.03
U1439C-34G-1-W 45-46	Cr-Sp	0.13	0.15	10.61	57.73	18.12	13.37	0.14	0.13	0.06	0.00
U1442A-56R-2-W 33-50	PLAG	49.81	0.00	31.37	0.00	0.65	0.24	0.03	0.00	15.33	2.38
U1442A-56R-2-W 33-50	PLAG	50.34	0.02	31.20	0.02	0.53	0.26	0.00	0.00	15.70	2.44
U1442A-56R-2-W 33-50	PLAG	51.37	0.03	31.20	0.00	0.61	0.24	0.03	0.00	15.36	2.27
U1442A-30R-3-W 121-122	PLAG	51.80	0.00	30.93	0.01	0.67	0.28	0.01	0.00	15.76	2.13
U1442A-30R-3-W 121-122	PLAG	50.41	0.02	31.38	0.00	0.66	0.31	0.00	0.00	16.22	2.42
U1442A-48R-1-W 97-98	PIG	53.88	0.02	2.82	0.84	7.03	23.30	0.13	0.01	11.47	0.09
U1442A-48R-1-W 97-98	PIG	54.43	0.14	2.08	0.30	9.21	26.15	0.12	0.03	7.07	0.10

[a] Minerals: Olivine (Ol), Cr-Spinel (Cr-SP), Enstatite (En), Clinoenstatite (CLEN), Pigeonite (PIG), Augite (AUG), Plagioclase

[b] Mineral end-member components: Enstatite (En), Wollastonite (Wo), Ferrosilite (Fs),Forsterite (Fo), Anorthite (An)

[c] Mg#=100*(Mg/(Mg+Fe)), Cr#= 100* (Cr/(Cr+Al))

888

889

Table 3. Unzoned Olivine Compositions

Sample	Mineral	SiO2 (wt%)	TiO2 (wt%)	Al2O3 (wt%)	Cr2O3 (wt%)	FeO (wt%)	MgO (wt%)	MnO (wt%)	CaO (wt%)	Na2O (wt%)	K2O (wt%)	
25R2	Ol Xeno	41.309	0.002	0.008	0.040	10.763	45.731	0.166	0.196	0.000	0.003	9
25R2	Ol Xeno	41.670	0.002	0.023	0.052	10.767	46.882	0.181	0.198	0.006	0.005	9
25R2	Ol Xeno	41.593	0.006	0.018	0.042	10.543	46.453	0.160	0.208	0.002	0.004	9
25R2	Ol Xeno	40.491	0.000	0.010	0.028	10.908	48.319	0.078	0.143	0.008	0.009	9
25R2	Ol Xeno OL	40.995	0.045	0.000	0.056	10.629	47.997	0.091	0.165	0.016	0.018	1
15R1	Pheno	40.555	0.000	0.000	0.017	12.994	46.926	0.077	0.170	0.000	0.000	1
15R1	OL	41.076	0.000	0.000	0.110	12.375	47.016	0.086	0.155	0.000	0.002	1

15R1	Pheno OL											
15R1	Pheno OL	41.703	0.001	0.068	0.290	11.586	46.450	0.190	0.159	0.125	0.123	1
15R1	Pheno OL	41.329	0.001	0.054	0.083	11.767	47.383	0.150	0.137	0.033	0.015	1
15R1	Pheno OL	40.664	0.002	0.019	0.064	11.810	47.674	0.157	0.140	0.004	0.000	1
19R2	Pheno OL	43.442	0.010	1.251	0.055	12.001	43.099	0.170	0.239	0.293	0.284	1
19R2	Pheno OL	41.978	0.000	0.012	0.061	10.441	48.192	0.217	0.157	0.000	0.000	1
2R3	Pheno OL	42.364	0.025	0.039	0.054	10.040	48.445	0.167	0.190	0.000	0.000	1
2R3	Pheno OL	42.247	0.000	0.021	0.115	10.944	48.009	0.196	0.115	0.018	0.011	1
		42.166	0.000	0.032	0.076	11.654	47.073	0.209	0.147	0.000	0.016	1

[a] Mineral: Olivine Xenocryst (Ol Xeno), Olivine Phenocryst (Ol Pheno).

[b] Samples: U1439C-25R-2-W 18-19 (25R2), U1439C-15R-1-W 8-10 (15R1), U1439C-19R-2-W 46-48 (19R2), U1439C-2R-3-

[c] Olivine End-member Components: Forsterite (Fo), Fayalite (Fa).

890

891

Table 1.
Typical Magma End-member Assembleges.

End member	Phenocrysts	Minor minerals	Matrix
HSB	Orthopyroxene ± Olivine	Cr-spinel	Clinopyroxene
LSB	Olivine + Orthopyroxene	Cr-spinel	Clinopyroxene ± Plagioclase
HMA	Plagioclase + Clinopyroxene	Magnetite + Ilmenite	Clinopyroxene + Plagioclase

[a] End-members: High-Si Boninite (HSB), Low-Si Boninite (LSB), High-Mg Andesite (HMA)

Table 2.

Normal Mineral Composition Observed in Magma Endmembers (Non-Mixing Samples).

Sample	Mineral	SiO2 (wt%)	TiO2 (wt%)	Al2O3 (wt%)	Cr2O3 (wt%)	FeO (wt%)	MgO (wt%)	MnO (wt%)	NiO (wt%)
U1439A-21X-1-W 2-3	En	57.18	0.00	0.67	0.42	7.70	32.33	0.07	0.07
U1439A-21X-1-W 2-3	En	56.44	0.00	1.19	0.61	8.74	31.68	0.09	0.10
U1439A-21X-1-W 2-3	CLEN	55.51	0.00	2.10	0.31	10.56	27.90	0.11	0.08
U1439A-21X-1-W 2-3	PIG	52.64	0.36	4.02	0.19	10.87	22.72	0.11	0.08
U1439A-21X-1-W 2-3	Cr-Sp	0.31	0.02	8.62	60.14	19.33	10.54	0.16	0.14
U1439A-21X-1-W 2-3	Cr-Sp	0.12	0.13	8.40	58.16	23.62	11.13	0.18	0.13
U1439C-33R-1-W, 137-140	Cr-Sp	0.13	0.08	9.71	56.72	19.36	13.48	0.30	0.00
U1439C-33R-1-W, 137-140	Ol	39.72	0.00	0.07	0.08	8.51	52.41	0.14	0.00
U1439C-29R-2-W 93-94	AUG	50.59	0.15	2.69	0.96	3.92	18.38	0.14	0.00
U1439C-29R-2-W 93-94	AUG	50.13	0.00	2.13	0.60	3.87	20.51	0.13	0.00
U1439C-34G-1-W 45-46	Ol	41.42	0.00	0.00	0.12	8.87	50.06	0.05	0.40
U1439C-34G-1-W 45-46	AUG	49.72	0.44	6.85	0.09	8.40	15.33	0.06	0.02
U1439C-34G-1-W 45-46	CLEN	56.03	0.00	1.40	0.76	8.90	29.19	0.10	0.04
U1439C-34G-1-W 45-46	CLEN	56.31	0.00	1.29	0.49	8.51	30.45	0.12	0.04
U1439C-34G-1-W 45-46	Cr-Sp	0.13	0.15	10.61	57.73	18.12	13.37	0.14	0.13
U1442A-56R-2-W 33-50	PLAG	49.81	0.00	31.37	0.00	0.65	0.24	0.03	0.00
U1442A-56R-2-W 33-50	PLAG	50.34	0.02	31.20	0.02	0.53	0.26	0.00	0.00
U1442A-56R-2-W 33-50	PLAG	51.37	0.03	31.20	0.00	0.61	0.24	0.03	0.00
U1442A-30R-3-W 121-122	PLAG	51.80	0.00	30.93	0.01	0.67	0.28	0.01	0.00
U1442A-30R-3-W 121-122	PLAG	50.41	0.02	31.38	0.00	0.66	0.31	0.00	0.00
U1442A-48R-1-W 97-98	PIG	53.88	0.02	2.82	0.84	7.03	23.30	0.13	0.01
U1442A-48R-1-W 97-98	PIG	54.43	0.14	2.08	0.30	9.21	26.15	0.12	0.03

[a] Minerals: Olivine (Ol), Cr-Spinel (Cr-SP), Enstatite (En), Clinoenstatite (CLEN), Pigeonite (PIG), Augite (AUG), Plag

[b] Mineral end-member components: Enstatite (En), Wollastonite (Wo), Ferrosilite (Fs),Forsterite (Fo), Anorthite (

[c] Mg#=100*(Mg/(Mg+Fe)), Cr#= 100* (Cr/(Cr+Al))

CaO (wt%)	Na2O (wt%)	K2O (wt%)	P2O5 (wt%)	Total (wt%)	Wo	En	Fs	Fo	An	Mg#	Cr#
1.24	0.04	0.01	0.00	99.73	2.38	86.12	11.50	-	-	88.22	29.34
1.54	0.02	0.00	0.00	100.39	2.93	84.06	13.01	-	-	86.60	25.60
4.27	0.05	0.00	0.00	100.89	8.32	75.62	16.06	-	-	82.48	8.95
9.85	0.09	0.02	0.00	100.94	19.72	63.29	16.98	-	-	78.84	3.00
0.04	0.00	0.01	0.00	99.31	-	-	-	-	-	49.28	82.39
0.06	0.05	0.00	0.00	101.97	-	-	-	-	-	45.64	82.29
0.12	0.09	0.00	0.00	99.99	-	-	-	-	-	55.37	79.67
0.15	0.02	0.01	0.00	101.12	-	-	-	91.65	-	91.65	44.28
23.16	0.17	0.00	0.00	100.14	44.71	49.38	5.90	-	-	89.32	19.31
23.00	0.20	0.03	0.00	100.59	42.16	52.30	5.54	-	-	90.42	15.82
0.14	0.00	0.00	0.00	101.05	-	-	-	90.96	-	90.96	100.00
18.15	0.17	0.03	0.00	99.27	39.42	46.34	14.25	-	-	76.49	0.88
3.59	0.04	0.00	0.00	100.04	7.01	79.40	13.59	-	-	85.39	26.84
2.81	0.03	0.02	0.00	100.06	5.42	81.76	12.82	-	-	86.44	20.46
0.06	0.00	0.00	0.00	100.44	0.17	56.72	43.11	-	-	56.82	78.50
15.33	2.38	0.05	0.00	99.87	-	-	-	-	87.53	39.56	-
15.70	2.44	0.02	0.06	100.58	-	-	-	-	87.64	46.80	0.04
15.36	2.27	0.52	0.04	101.66	-	-	-	-	86.68	41.62	0.00
15.76	2.13	0.25	0.08	101.91	-	-	-	-	88.35	42.75	0.02
16.22	2.42	0.05	0.00	101.47	-	-	-	-	87.98	45.61	-
11.47	0.09	0.00	0.00	99.60	23.23	65.66	11.11	-	-	85.53	16.71
7.07	0.10	0.00	0.03	99.64	13.96	71.84	14.20	-	-	83.50	8.78

gioclase (PLAG).

An)

Table 3.

Unzoned Olivine Compositions

Sample	Mineral	SiO_2 (wt%)	TiO_2 (wt%)	Al_2O_3 (wt%)	Cr_2O_3 (wt%)	FeO (wt%)	MgO (wt%)	MnO (wt%)	CaO (wt%)
25R2	Ol Xeno	41.309	0.002	0.008	0.040	10.763	45.731	0.166	0.196
25R2	Ol Xeno	41.670	0.002	0.023	0.052	10.767	46.882	0.181	0.198
25R2	Ol Xeno	41.593	0.006	0.018	0.042	10.543	46.453	0.160	0.208
25R2	Ol Xeno	40.491	0.000	0.010	0.028	10.908	48.319	0.078	0.143
25R2	Ol Xeno	40.995	0.045	0.000	0.056	10.629	47.997	0.091	0.165
15R1	OL Pheno	40.555	0.000	0.000	0.017	12.994	46.926	0.077	0.170
15R1	OL Pheno	41.076	0.000	0.000	0.110	12.375	47.016	0.086	0.155
15R1	OL Pheno	41.703	0.001	0.068	0.290	11.586	46.450	0.190	0.159
15R1	OL Pheno	41.329	0.001	0.054	0.083	11.767	47.383	0.150	0.137
15R1	OL Pheno	40.664	0.002	0.019	0.064	11.810	47.674	0.157	0.140
15R1	OL Pheno	43.442	0.010	1.251	0.055	12.001	43.099	0.170	0.239
19R2	OL Pheno	41.978	0.000	0.012	0.061	10.441	48.192	0.217	0.157
19R2	OL Pheno	42.364	0.025	0.039	0.054	10.040	48.445	0.167	0.190
2R3	OL Pheno	42.247	0.000	0.021	0.115	10.944	48.009	0.196	0.115
2R3	OL Pheno	42.166	0.000	0.032	0.076	11.654	47.073	0.209	0.147

[a] Mineral: Olivine Xenocryst (Ol Xeno), Olivine Phenocryst (Ol Pheno).

[b] Samples: U1439C-25R-2-W 18-19 (25R2), U1439C-15R-1-W 8-10 (15R1), U1439C-19R-2-W 46-48 (19R2),

[c] Olivine End-member Components: Forsterite (Fo), Fayalite (Fa).

Na2O (wt%)	K2O (wt%)	Total (wt%)	Fo	Fa
0.000	0.003	98.218	88.337	11.663
0.006	0.005	99.786	88.587	11.413
0.002	0.004	99.028	88.706	11.294
0.008	0.009	99.994	88.759	11.241
0.016	0.018	100.012	88.950	11.050
0.000	0.000	100.739	86.555	13.445
0.000	0.002	100.820	87.134	12.866
0.125	0.123	100.695	87.725	12.275
0.033	0.015	100.951	87.772	12.228
0.004	0.000	100.534	87.798	12.202
0.293	0.284	100.843	86.489	13.511
0.000	0.000	101.058	89.163	10.837
0.000	0.000	101.324	89.585	10.415
0.018	0.011	101.676	88.662	11.338
0.000	0.016	101.373	87.805	12.195

, U1439C-2R-3-W 2-3 (2R3).

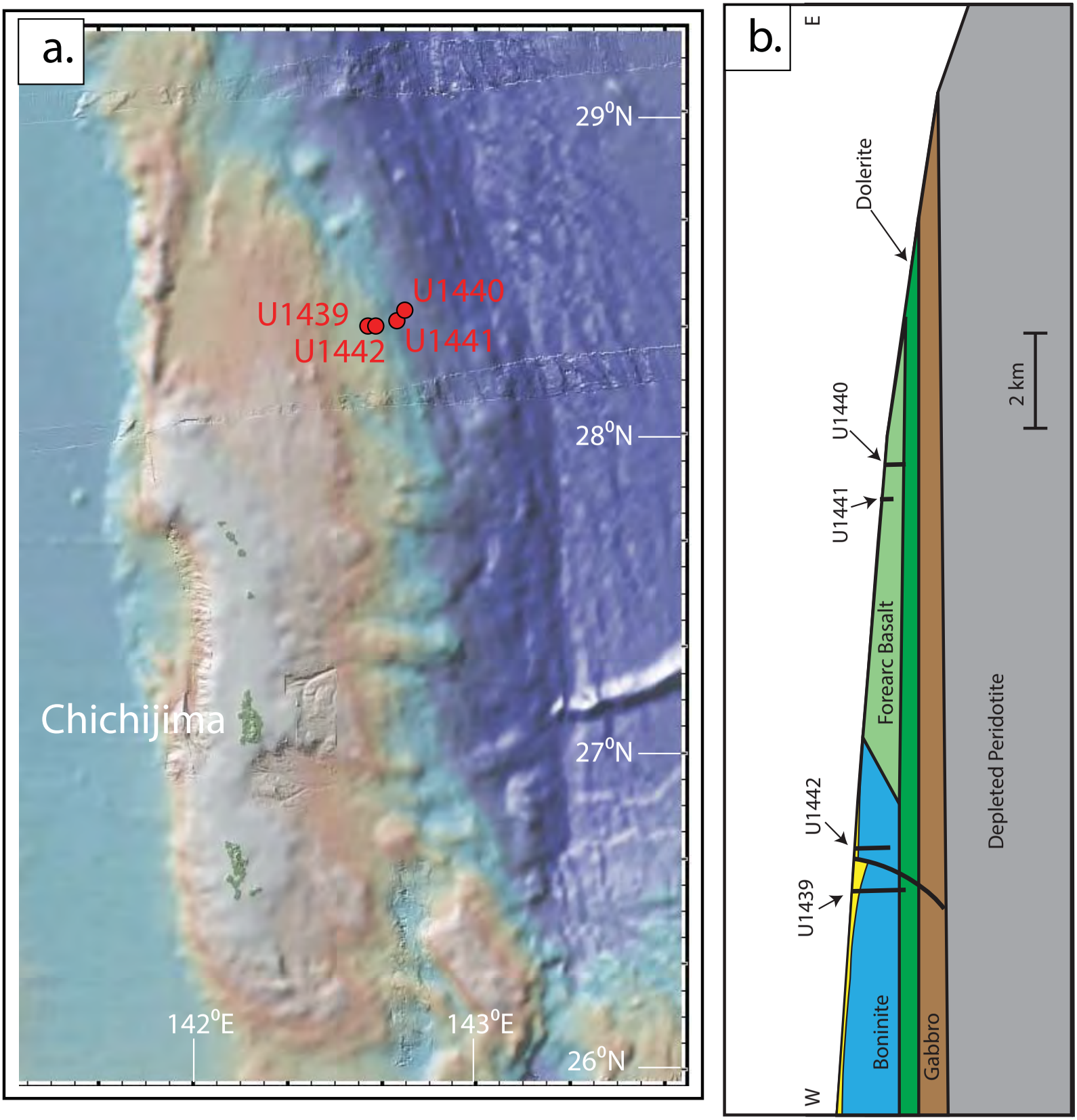
a.
29°N
28°N
27°N
26°N
142°E
143°E
U1440
U1439
U1441
U1442
Chichijima
b.
E
W
Dolerite
U1440
U1441
U1442
U1439
Forearc Basalt
Boninite
Gabbro
Depleted Peridotite
2 km

Figure 1

Boninite Group

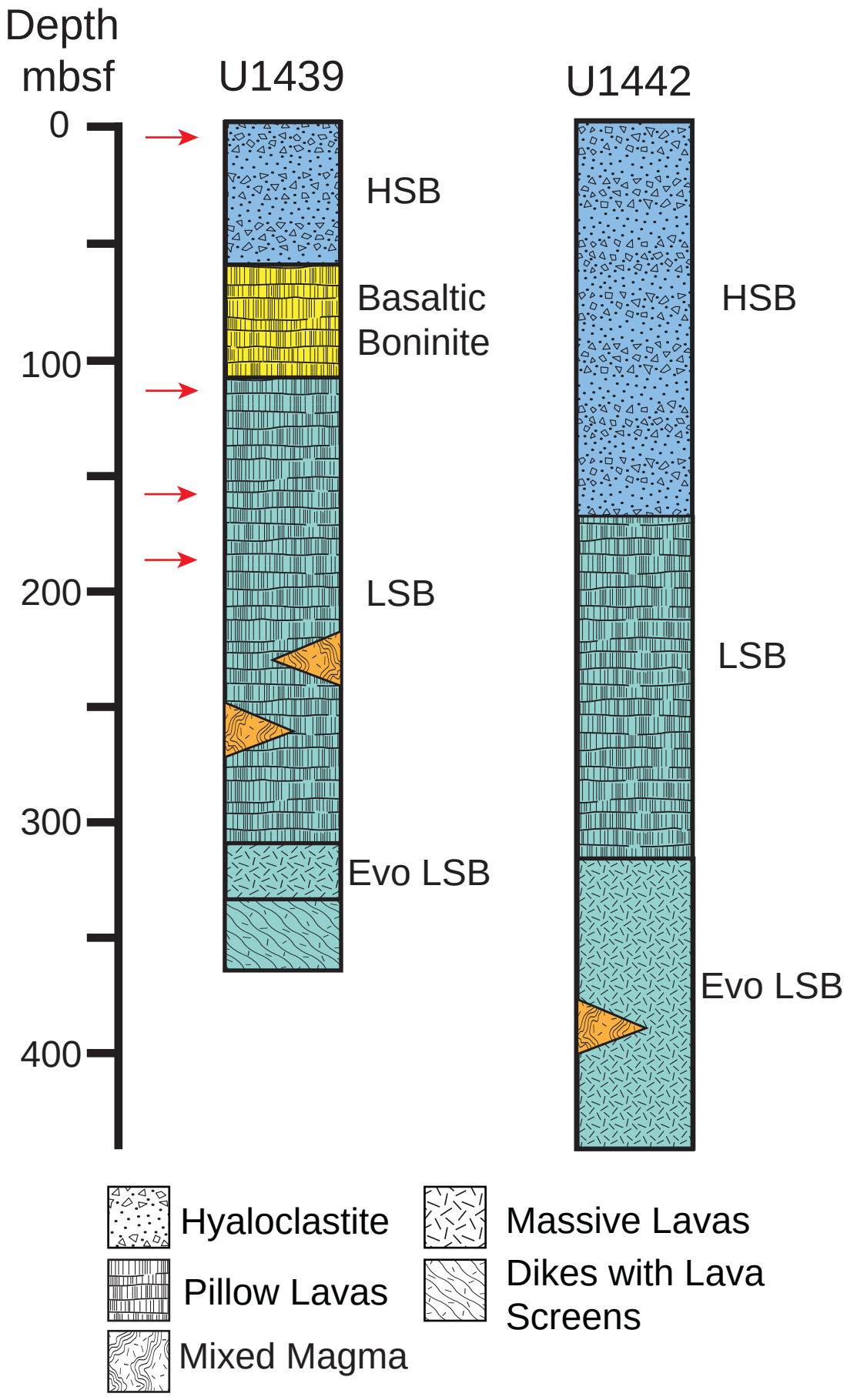

Figure 2

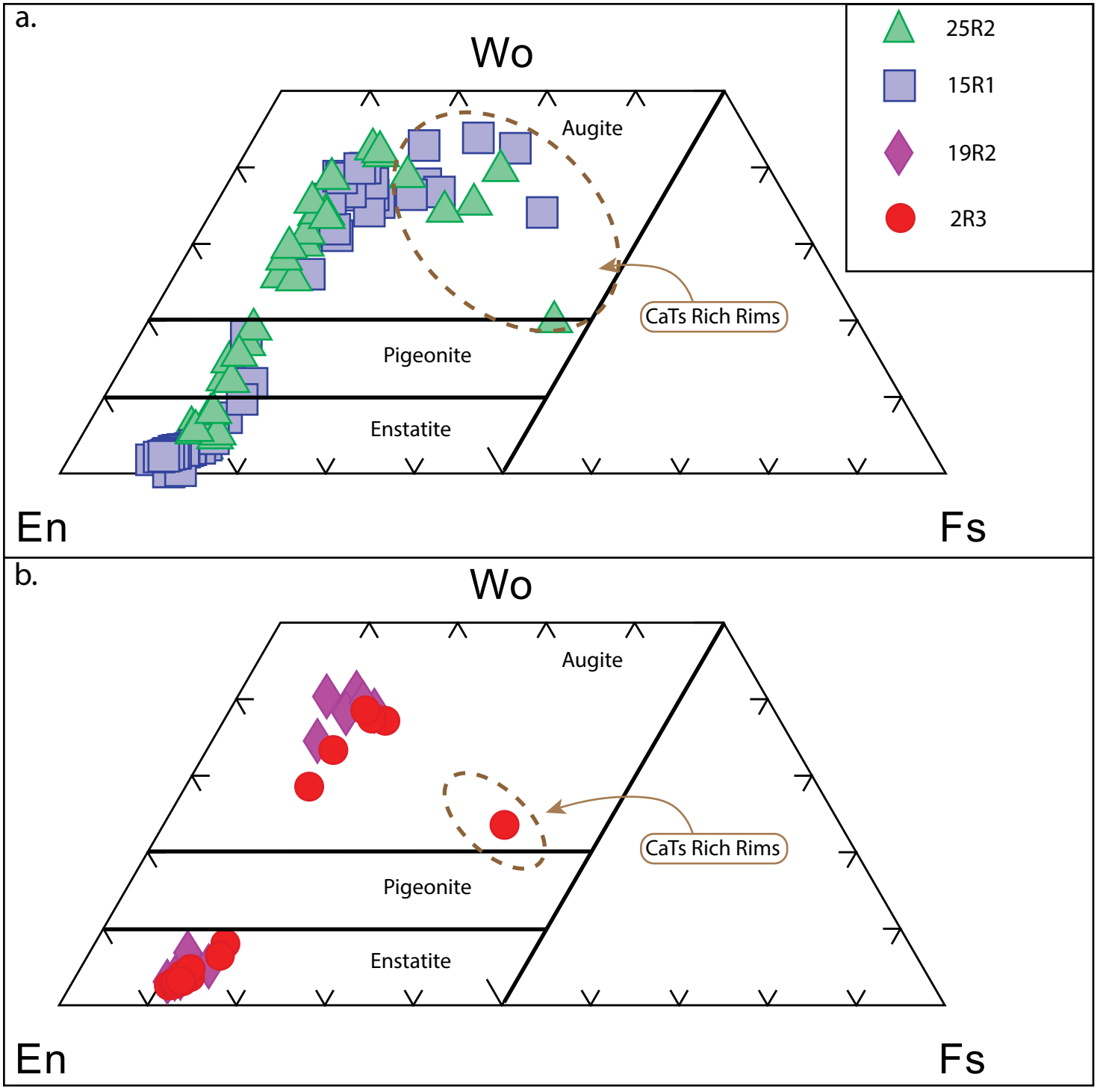
a.
Wo
Augite
CaTs Rich Rims
Pigeonite
Enstatite
En
Fs
25R2
15R1
19R2
2R3
b.
Wo
Augite
CaTs Rich Rims
Pigeonite
Enstatite
En
Fs

Figure 3

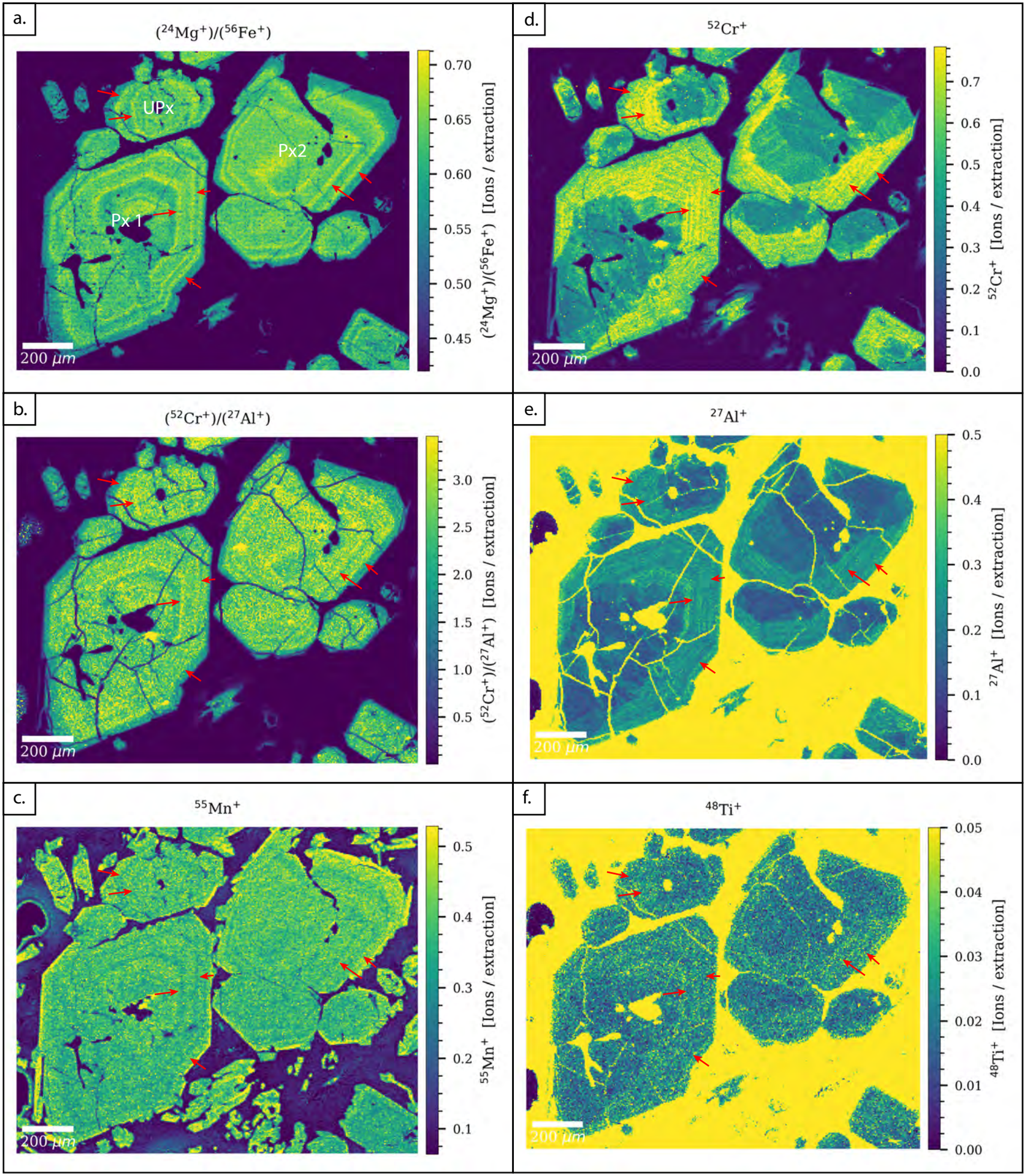
a.
$(^{24}Mg^+)/(^{56}Fe^+)$
UPx
Px2
Px 1
200 µm
0.70
0.65
0.60
0.55
0.50
0.45
$(^{24}Mg^+)/(^{56}Fe^+)$ [Ions / extraction]
d.
$^{52}Cr^+$
200 µm
0.7
0.6
0.5
0.4
0.3
0.2
0.1
0.0
$^{52}Cr^+$ [Ions / extraction]
b.
$(^{52}Cr^+)/(^{27}Al^+)$
200 µm
3.0
2.5
2.0
1.5
1.0
0.5
$(^{52}Cr^+)/(^{27}Al^+)$ [Ions / extraction]
e.
$^{27}Al^+$
200 µm
0.5
0.4
0.3
0.2
0.1
0.0
$^{27}Al^+$ [Ions / extraction]
c.
$^{55}Mn^+$
200 µm
0.5
0.4
0.3
0.2
0.1
$^{55}Mn^+$ [Ions / extraction]
f.
$^{48}Ti^+$
200 µm
0.05
0.04
0.03
0.02
0.01
0.00
$^{48}Ti^+$ [Ions / extraction]

Figure 4

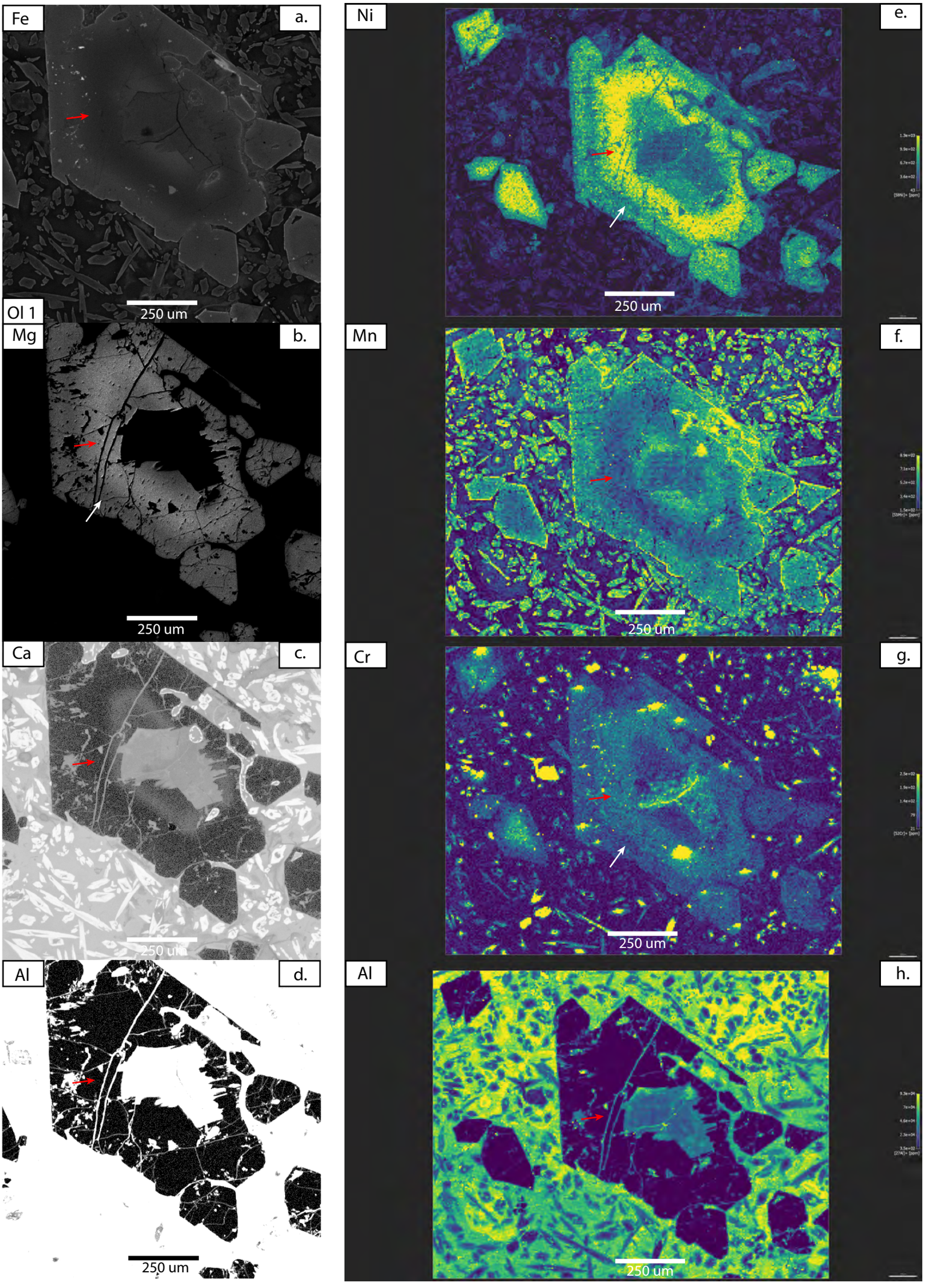
Fe
a.
250 um
Ol 1
Mg
b.
250 um
Ca
c.
250 um
Al
d.
250 um
Ni
e.
250 um
Mn
f.
250 um
Cr
g.
250 um
Al
h.
250 um

Figure 5

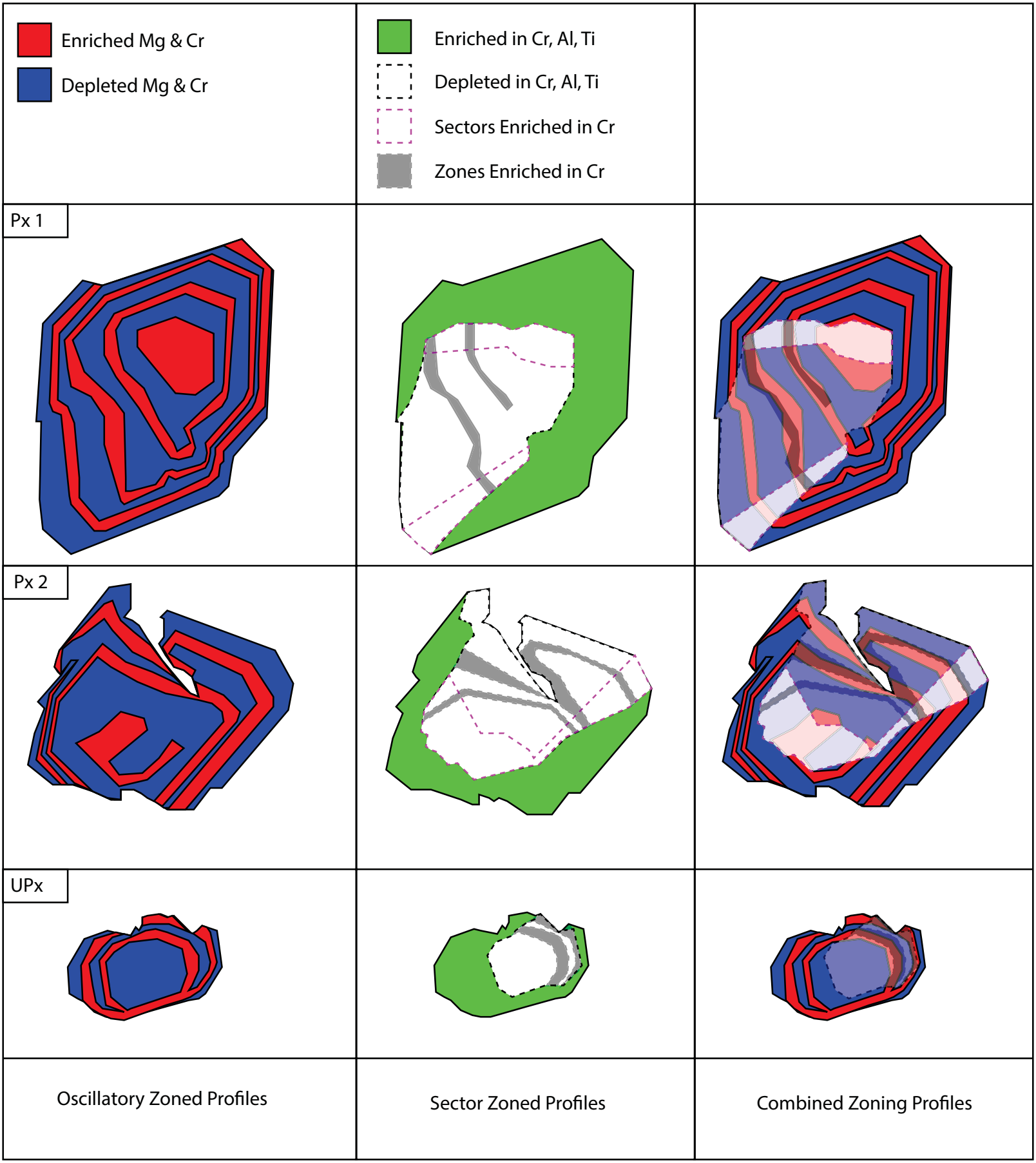
Enriched Mg & Cr
Depleted Mg & Cr
Enriched in Cr, Al, Ti
Depleted in Cr, Al, Ti
Sectors Enriched in Cr
Zones Enriched in Cr
Px 1
Px 2
UPx
Oscillatory Zoned Profiles
Sector Zoned Profiles
Combined Zoning Profiles

Figure 6

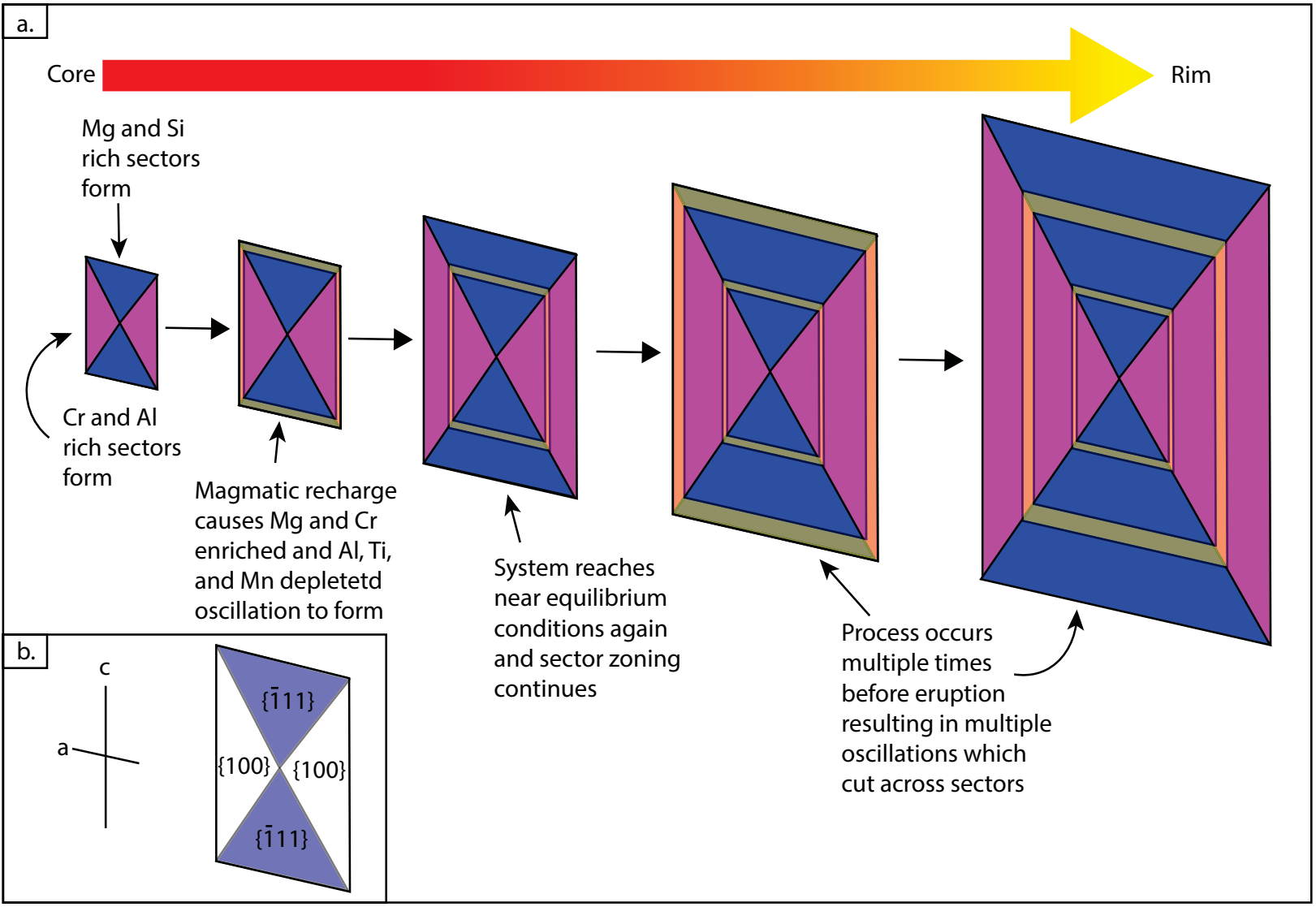
a.
Core
Rim
Mg and Si rich sectors form
Cr and Al rich sectors form
Magmatic recharge causes Mg and Cr enriched and Al, Ti, and Mn depletetd oscillation to form
System reaches near equilibrium conditions again and sector zoning continues
Process occurs multiple times before eruption resulting in multiple oscillations which cut across sectors
b.
c
a
{$\bar{1}$11}
{100}
{100}
{$\bar{1}$11}

Figure 7

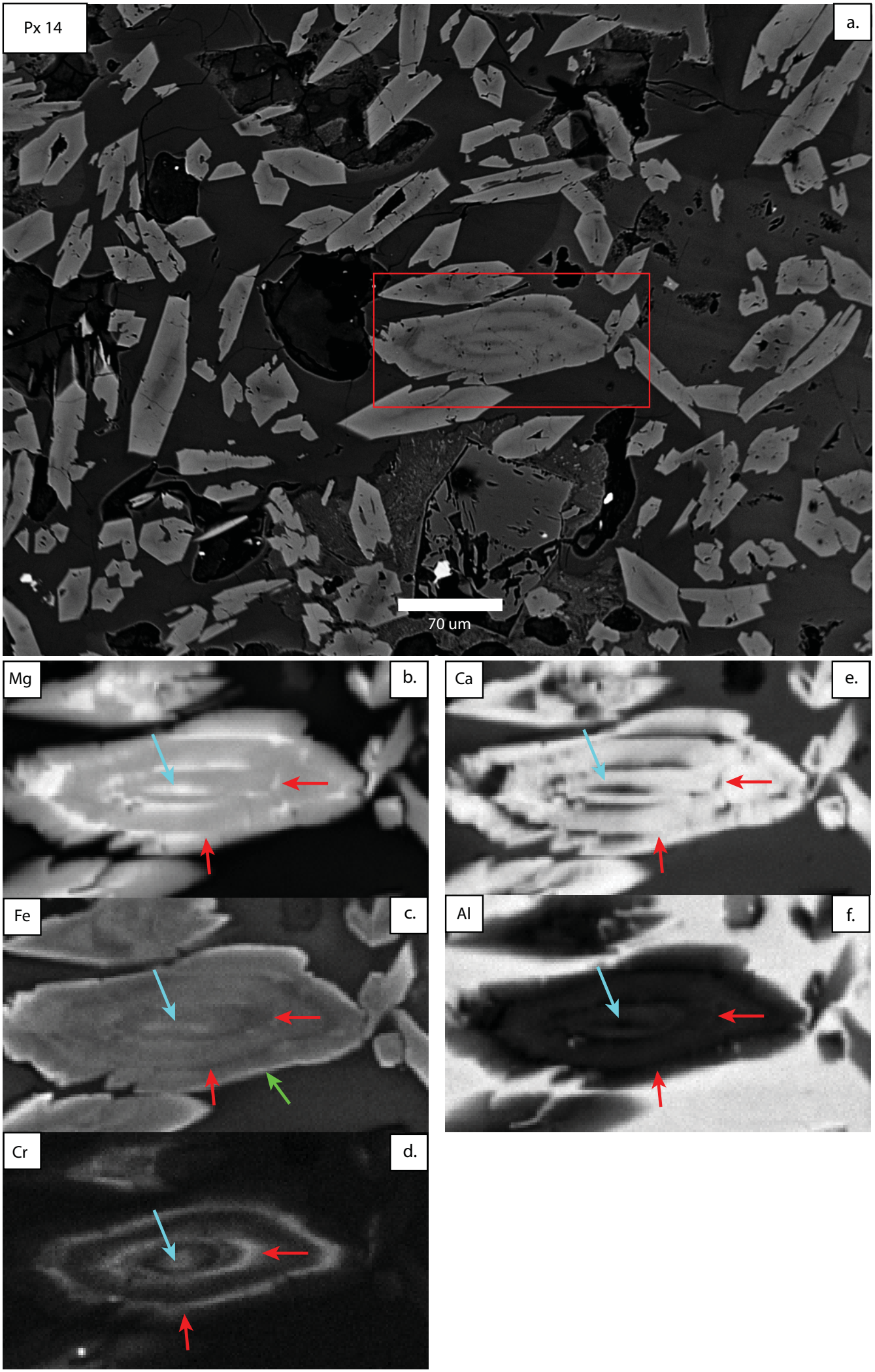
Px 14
a.
70 um
Mg
b.
Fe
c.
Cr
d.
Ca
e.
Al
f.

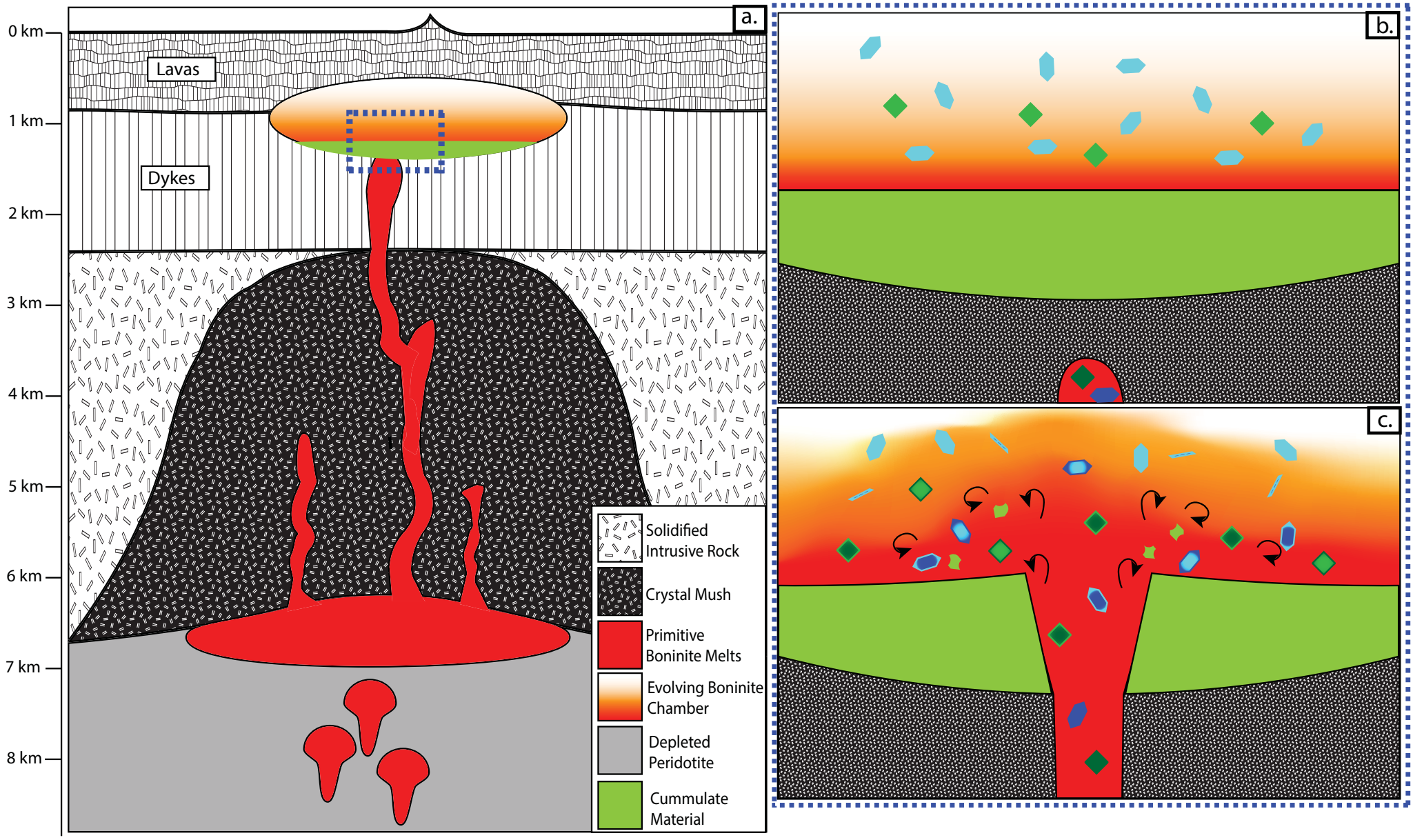
a.
b.
c.
0 km
1 km
2 km
3 km
4 km
5 km
6 km
7 km
8 km
Lavas
Dykes
Solidified Intrusive Rock
Crystal Mush
Primitive Boninite Melts
Evolving Boninite Chamber
Depleted Peridotite
Cummulate Material

Figure 9